LBL-26319 c.2

# Lawrence Berkeley Laboratory
UNIVERSITY OF CALIFORNIA

## Materials & Chemical Sciences Division

National Center for Electron Microscopy

RECEIVED
LAWRENCE
BERKELEY LABORATORY

APR 26 1989

LIBRARY AND
DOCUMENTS SECTION

Invited paper presented at the American Ceramic Society
Pacific Meeting, San Francisco, CA, October 26–28, 1988

# Atomic Imaging and Microanalysis of Ceramics

G. Thomas and R. Ramesh

October 1988

TWO-WEEK LOAN COPY

This is a Library Circulating Copy
which may be borrowed for two weeks.

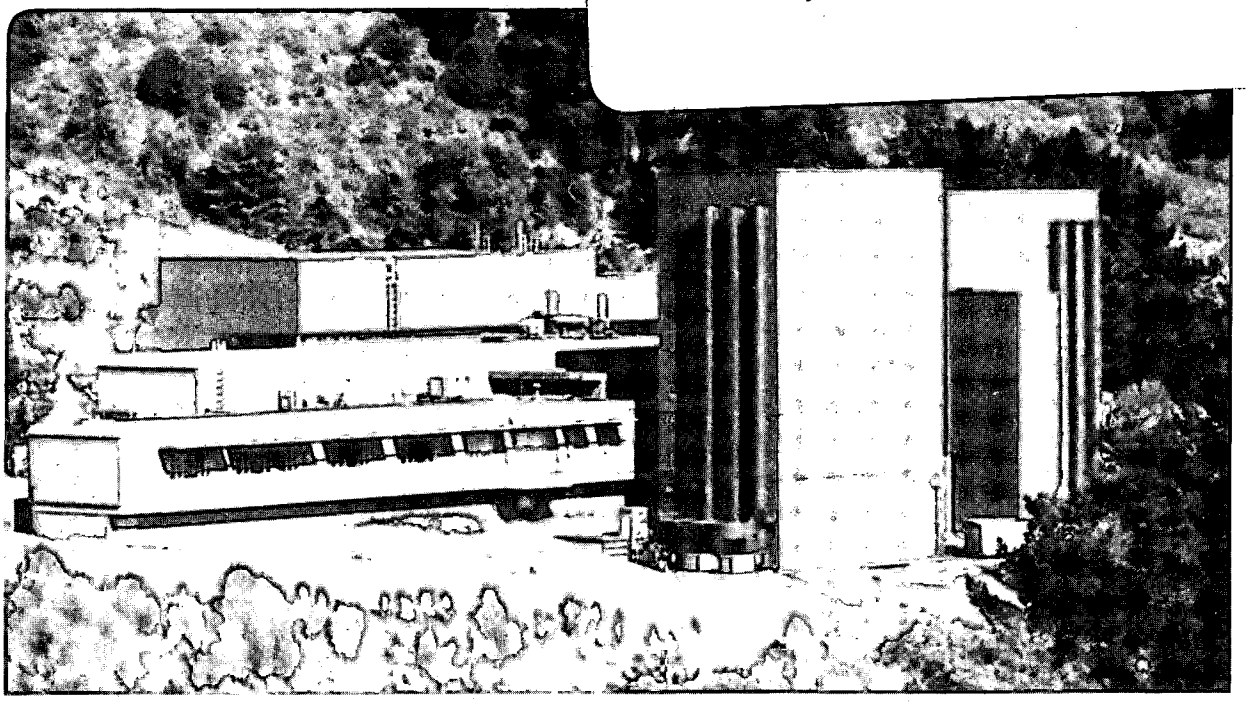

LBL-26319 c.2

Prepared for the U.S. Department of Energy under Contract Number DE-AC03-76SF00098.

## DISCLAIMER

This document was prepared as an account of work sponsored by the United States Government. While this document is believed to contain correct information, neither the United States Government nor any agency thereof, nor the Regents of the University of California, nor any of their employees, makes any warranty, express or implied, or assumes any legal responsibility for the accuracy, completeness, or usefulness of any information, apparatus, product, or process disclosed, or represents that its use would not infringe privately owned rights. Reference herein to any specific commercial product, process, or service by its trade name, trademark, manufacturer, or otherwise, does not necessarily constitute or imply its endorsement, recommendation, or favoring by the United States Government or any agency thereof, or the Regents of the University of California. The views and opinions of authors expressed herein do not necessarily state or reflect those of the United States Government or any agency thereof or the Regents of the University of California.

# ATOMIC IMAGING AND MICROANALYSIS OF CERAMICS

**G.Thomas and R.Ramesh**
Department of Materials Science and Mineral Engineering,
University of California, Berkeley and National Center for Electron Microscopy,
Materials and Chemical Sciences Division, Lawrence Berkeley Laboratory, 1
Cyclotron Road, Berkeley
CA 94720.

## INTRODUCTION

The inherent complexity of the crystal structure and microstructure of ceramics and the inter-dependence of the final properties on microstructure and processing, means that detailed characterization of the effect of processing variables on the structure and microstructure is imperative. Thus in order to understand and improve ceramics it is necessary to establish these relationships iteratively. One common theme in this research methodology is the characterization of the grain boundaries and the structural and microchemical changes that take place near such interfaces. Electron microscopy has become firmly established as a powerful analytical tool for the characterization of the structure and microstructure in ceramics research. Due to the various types of interactions of electrons with materials the electron microscope is unique in that it can provide morphological, structural and chemical information with high spatial resolution. **Fig.1** shows the various types of information that can be obtained from a modern transmission electron microscope. However, one has to be aware of some of the inherent problems associated with electron microscopy of ceramic materials. These are : (i) specimen preparation for electron microscopy and the possible changes in the nature of the sample due to thin foil effects ; (ii) radiation damage, especially knock-on damage ; (iii) image resolution of anions.

## IMAGING AND XRAY SPECTROSCOPY

It has long been the goal of electron microscopists to achieve interpretable atomic resolution. For thin enough crystals, the weak phase object approximation can be made, which implies that the image is basically a projection of the lattice potential. Hence contrast of atomic columns is proportional to the projected atomic number along that column. The resolution is fundamentally a function of the electron wavelength and lens aberrations, especially spherical aberration, quantified by the relationship : $R = 0.66C_S^{1/4}\lambda^{3/4}$, which is plotted in **Fig.2**[1]. As shown in this figure, to achieve 2Å point resolution using an objective lens with $C_S$ =3mm, one would have to operate in the range of 600-1000kV. Thus, with increasing energy, the reduction in the wavelength enables interpretable atomic resolution to be achieved when approaching 1MeV. In addition, the effect of chromatic aberration is reduced by increasing the accelerating voltage, since this parameter varies as $(kV)^{-1}$. Another resolution limit is set by the ultimate cut-off spectra due to instrumental instabilities. The effects of aberrations and defocus of the abjective lens must be taken into account when considering the ability of the lens to transfer sufficient "in-phase" information scattered within the lens aperture that can provide such phase contrast to yield interpretable structure imaging. The phase shift between a scattered and un-deviated electron beam is given by :

$$\chi(\alpha) = \pi/\lambda[(C_S.\alpha^4)/2 + D.\alpha^2] = \pi.\lambda.g^2(C_S.\lambda^2g^2/2) + D \quad (1)$$

for Bragg scattering where $\lambda.g = 2\theta$, $\alpha = 2\theta$ and D = objective lens defocus. The lens thus transfers information as a complex quantity $i.\chi(g)$ which can be represented as a diagram of $(\chi)$ vs. g for varying $C_S$ and D. Damping terms can also be included to account for chromatic errors, beam divergence, mechanical noise, etc. This plot is known as the contrast transfer function (CTF), e.g., **Fig.3(a)**. The phase contrast at high resolution is the imaginary part of the CTF. It can be seen that the objective lens defocus offsets the loss in resolution due to $C_S$.

The value of the optimum defocus is known as the Scherzer defocus, obtained by differentiating the CTF and setting $\chi(g) = -\pi/2$ and has the result : $D_{Sch} = -(C_s.\lambda)^{1/2}$. From Fig.3(a), it is seen that the resolution of the Berkeley ARM ( at 1000kV) of ~1.4Å is the best currently available in the world, along with the ±40° specimen tilt. The resolution of the 400kV microscopes, Fig.3(a), which are based on the design of the ARM is about 1.7Å. Of course when a specimen is introduced into the problem, then one must also consider parameters such as thickness, as illustrated by the example in Fig.3(b). In this figure computed images for orthorhombic $ZrO_2$ are shown for different values of foil thickness and defocus(2). It is to be noted that the detail available is very different from one image to another. These considerations show that atomic resolution images cannot be interpreted by mere inspection. This must be done via the use of known operating parameters of the microscope and specimen and involves sophisticated computing in addition to expert microscopy.

At the National Center for Electron Microscopy (NCEM), the atomic resolution microscope (ARM) has been designed to meet the above requirements over its entire voltage range of 400kV to 1000kV at constant $C_s.\lambda$. The key to this variable voltage atomic resolution performance is the top entry specimen stage that, in addition to ±40° tilting, can be moved up and down in order to maintain a constant value of $C_s.\lambda$ for a given value of objective lens current(3). Additionally, this enables tuning of the voltage to below the threshold for knock-on damage, especially for beam sensitive materials such as ceramic oxides and glasses. The key to successful interpretation of atomic resolution images is the computing and image simulation facilities that are available at the center. Such facilities provide very rapid feedback to the researcher, enabling quick and effective optimization of the imaging conditions. The image processing facility is similar to that described by Saxton and Koch(4). For image simulation, the new program, NCEMSS( National Center for Electron Microscopy Simulation Software) provides an interactive milieu via a mouse input. Details of the computing facilities are given in earlier references(5,6). In association with the image processing computer, a second computer system has been designed to acquire and enhance electron microscope images in real time at video rates from three microscopes. This real time system allows the user to make necessary optical adjustments e.g., astigmatism, in less than a minute thus limiting the delay resulting from improper imaging conditions.

Analytical electron microscopy forms the other important facet to modern electron microscopy since it provides spectroscopic and diffraction information from the regions being examined. With the use of energy dispersive xray spectroscopy (EDXS) and electron energy loss spectroscopy (EELS), it is possible to obtain full quantitative chemical information for all elements above Z=5, with a spatial resolution of about 100Å. Likewise, microdiffraction and convergent beam electron diffraction, provide structural information with a spatial resolution approaching 40Å ( determined by the probe size) for a $LaB_6$ filament. This, however, can be improved by the use of a higher coherence source such as the field emission gun(FEG), which, unfortunately, is not widely available and none at present above 200kV. Atomic level resolution can be indirectly obtained by using techniques such as ALCHEMI(7). Since the optimum microscope requirements are not the same for these different techniques, it is essential that each microscope is dedicated to a specific collection of tasks, e.g., atomic resolution imaging, microanalysis, magnetic imaging. The NCEM is such a dedicated instrument facility.

In the following, examples from on-going research at Berkeley are presented that illustrate the application of atomic resolution imaging, image simulation and processing and microanalysis towards understanding modern ceramics.

## A. High $T_c$ oxide superconductors

The recent discovery of superconductivity above 100K in Bi-Ca-Sr-Cu-O has further fueled the excitement prevailing in this area of research since the discovery of "warm" ceramic superconductors such as Y-Ba-Cu-O(8). The superconducting

phase in this system, described by the general composition of $Bi_2Sr_2Cu_nCa_{n-1}O_y$, exhibits polytypoid-like behaviour[9], similar to other well-known oxide ceramics. The $T_c$ is known to increase with "n", the number of Cu-O layers. The stacking sequence in these complex oxides has been revealed by atomic resolution imaging[10]. In **Fig.4(a)**, a [110] ARM image of the n=3 ( $T_c$ =110K) polytypoid is shown. Since the projection of the atomic potential is imaged, the images of the Bi atoms ( Z=83) are the largest, while that of Ca the smallest. Note that this can also be used to obtain atomic discrimination, i.e., replacement of Ca by Bi ( their ionic radii are almost the same) can be directly identified. The SEMPER processed image in **Fig.4(b)** shows another interesting detail of the structure. The contrast corresponding to the central Cu-O layer ( indicated by arrows) is quite different from that of the other two rows, suggesting a deficiency of oxygen along that "chain". Image simulations confirm this inference. In **Figs.5(a&b)** the [110] projected potential and a series of simulated images are shown respectively for the perfect crystal. In **Figs.5(c&d)** the same are shown for a crystal in which the oxygen atoms from the central Cu-O row are removed. In the simulated image in (d), the contrast of the central Cu-O row is different from that of the other two rows, as seen in the processed image in **Fig.4(b)**.

High resolution imaging, in conjunction with EDX microanalysis, has also shown that in these solid state processed samples, the grain boundaries are Cu and Ca deficient, thus causing the lower $T_c$ n=1 or 2 polytypoid to form. **Fig.6(a)** is a lattice fringe image showing the polytypoid structures adjacent to the grain boundary. The $T_c$ values decrease towards the grain boundary due to the change in the composition and $T_c$ for each polytypoid. **Fig.6(b)** is a typical lattice fringe image of a sample with PbO added, showing a uniform n=3 structure upto the grain boundary. The resistivity plot of the leaded samples are quite different from those of the unleaded samples[9]. Similar effects have been observed in Mg-SiAlONs, **Fig.7**, in which the cation:anion ratio changes close to the grain boundary, causing the formation of different polytypes[11]. In another example, Be-Si-N[12], the formation of different polytypic structures occurs by the propagation of a stacking fault through the lattice. **Fig.8** shows a typical example where HREM, in conjunction with image simulation has been used to identify different polytypoid structures. While the effect of such changes near grain boundaries in MgSiAlONs on their properties is not clear, it is very likely that the low $T_c$ polytypoids adjacent to the grain boundaries can affect intergranular "connectivity"[13]. Another aspect of concern is the nature of the grain boundary plane itself. In the case of Y-Ba-Cu-O, high resolution imaging of the grain boundaries has shown that approximately 70% of the grain boundaries planes are of the (001) type. **Fig.9(a)** shows one such typical grain boundary, in which the upper grain is in the [100] zone and the lower in the [441] zone[14]. In **Fig.9(b)** is shown a SEMPER processed image in which only the upper grain has been processed. The interesting feature in this image is that the grain boundary plane is a BaO plane. It is well known that BaO is an insulator, and hence is likely to be a barrier to the movement of the super-current from one grain to another, especially if this plane is an inherent feature of the structure of the grain boundary. In the case of the BCSCO ceramics, the grain boundary plane is generally a Bi-O plane.

These alkali earth based ceramics are typical examples in which the effect of the electron beam on the integrity of the sample is pronounced. **Fig.10** is an example of the BCSCO sample irradiated with an 800kV electron beam. The edge of the foil is completely damaged due to knock-on damage. This is one problem that needs to be kept in mind when imaging such materials. The operator needs to be extremely efficient and fast in order to acquire the images. On the other hand, dynamic acquisition of the images on a magnetic tape could turn out to be useful.

## B. Mullite-zirconia ceramics

Incorporation of zirconia particles in a mullite matrix has been found to beneficially improve the fracture toughness. There has been considerable debate over the structure of mullite, especially regarding the ordering of

vacancies[15,16]. This may, in part, be due to the large range of solid solubility in the $Al_2O_3$-$SiO_2$ system. Similarly, several different structural variants of zirconia, including ordered structures, have been observed, e.g., the orthorhombic form shown in **Fig.3(b)**[2]. Atomic resolution imaging, in conjunction with image simulations and matching, has been utilized to understand the structure of these two phases. **Fig.11** shows the structural model of mullite that was used in the simulations. EDX microanalysis showed small amounts of Ti in solid solution ( due to the reaction sintering). The $Al_2O_3$-$SiO_2$-$TiO_2$ phase diagram shows a shift in the composition of mullite from the ideal 3:2 ($Al_2O_3$:$SiO_2$) to the 2:1 composition. For the samples used in this study the ratio was found to be 1.7:1. **Figs.12(a&b)** show simulated images of a 29 Å mullite crystal for defocus values of 0Å and 100Å respectively. The corresponding ARM image is shown in **Fig.12(c)**. The match between the experimental and simulated images is very good, thus verifying the structure model. It may be noted that there is no evidence for any ordering, although other orientations must be explored before this matter can be unequivocally settled. **Figs.13(a&b)** show simulated images for a 87Å thick foil at defocus values of 0Å and 100Å and the match with the experimental image, **Fig.13(c)** is very good. The drastic change in the nature of the images, with thickness and defocus, makes it imperative that image interpretation be carried out only with the assistance of thorough image simulation and matching. This is illustrated by the strong influence on the image details of a small tilt of the sample from the exact zone axis. This influence can be recognized by obtaining the Fourier transform of the image using the SEMPER program. **Fig.14(a)** shows the actual image of mullite, with the corresponding optical diffraction pattern shown in **Fig.14(b)**. In this pattern , it can be seen that the intensity of the diffraction spots is not the same, indicating a small tilt of the foil. This can however, be corrected for in the computer, to produce the zone axis image. The results of this are shown in **Figs.14(c&d)**. **Fig.14(c)** is the image of the same region as in **Fig.14(a)**, but with the sample in the exact zone. The corresponding optical diffraction pattern is shown in **Fig.14(d)**. This example clearly illustrates the critical need for a large tilt range (e.g., ±40°), to enable the operator to tilt the sample into the exact zone axis with the assistance of on-line computer analysis. It also illustrates the capability of currently existent software and hardware to assist the operator in obtaining the optimum information from the microscope. With the advent of dynamic microscope-computer interactions in the near future, such experiments will be possible as the operator is working at the microscope, rather than after the experiment. This will enable the correction of imaging conditions to be done instantaneously.

## C.Crystallization of glasses in Y-SiAlONs

Much research has been carried out on SiAlONs with small amounts of sintering additives such as $Y_2O_3/Al_2O_3$, MgO, etc. to enhance densification[17-21]. This leads to liquid phase sintering, consequent to which the liquid phase does not completely crystallize. **Figs.15(A-E)** show different intergranular configurations after liquid phase sintering. The most desirable microstructure is that in "D", where all the liquid phase has crystallized or that in "E" where all additives are taken into solution in the matrix, provided no polytypes ( or polytypoids) such as in **Fig.6(a), Fig.7**, and **Fig.8**, form. The amorphous phase that forms due to the solidification of the liquid phase, is detrimental to the high temperature properties of the ceramic. Electron microscopy and microanalysis have been instrumental in understanding these intergranular phases. Since this problem was observed in the case of many additives, a research program addressing the crystallization characteristics of a ceramic of composition equal to that of the amorphous phase was started in Berkeley in 1980,[see ref.(22)]. These compositions are shown in the isothermal section of the AlN-$SiO_2$-$Y_2O_3$ phase diagram in **Fig.16**. At 1000°C, dendritic nucleation occurs on heterogeneous sites with the formation of an orthorhombic "y" phase polymorphic with the $Y_2Si_2O_7$ phase. HREM and atomic resolution imaging have been used to examine the details of the different polytypes

or polytypoids that form during the crystallization process. It has been observed that the crystallization proceeds via the formation of an intermediate $\delta_1$ phase, which is heavily faulted. The side-arms in this growth structure are close to equilibrium $Y_2Si_2O_7$ and grow epitaxially as one of the twin variants. The details of this structure are shown in the HREM image in **Fig.17(a)**[23]. This image shows the nature of the interface between the $\delta_1$-$\delta_2$ dendrites. The flat interfaces are twin boundaries with strain contrast only at the ledges. The atomic configurations of the different phases appearing upon crystallization are not very different. In such cases, direct imaging along with image matching is extremely useful in identifying the phase. In **Fig.17(b)**, an ARM image of the $\delta_1$ $Y_2Si_2O_7$ phase is shown along with the simulated image[24]. The match between the experimental and simulated image is very good except for the slight skew of the image, probably due to a slight specimen tilt. These crystallization processes proceed with the rejection of Al and N ahead of the transformation interface, as evidenced by EDX microanalysis. Upon prolonged annealing, it is possible to achieve complete crystallization. As in the case of mullite, the image details in this system are sensitive to small misorientations and interpretation is possible only for extremely thin sections. However, in the case of these crystallized glasses, the thinnest areas are generally found near the amorphous regions. Thus, the image details are convoluted with the contribution from the amorphous phase. The crystalline details in the thinnest part of the image can be deconvoluted using the SEMPER program, the results of which are shown in **Figs.18(a-d)**[25]. In the region of the sample near the amorphous phase, the structural details cannot be readily identified, as illustrated in **Fig.18(a)**. In the thicker parts of the sample, **Fig.18(b)**, more structural information is available, although not directly interpretable as projections of the atomic potential. In addition, details of the symmetry of the crystal are not obvious from this image. The structural information in the image in **Fig.18(a)** can be obtained by deconvolution of the amorphous background by image processing. **Fig.18(c)** shows the SEMPER processed image. The processing was carried out by obtaining the Fourier transform, followed by filtering using apertures around each intensity maximum in the Fourier transform. This filtered Fourier transform was subsequently reversed to obtain the filtered images in **Fig.18(c&d**. In Fig.18(e) the processed image from the thin region is over-laid on the simulated image, and shows an excellent match. The capability of such image processing techniques for deconvoluting the effect of the influence of an amorphous phase, whether it is an inherent part of the sample or produced due to the sample preparation method, is clearly illustrated in this example.

**D. Al-O-Ns**

Another related area of research is that of Al-O-Ns. It has been suggested that the study of the much simpler system $Al_2O_3$-AlN would provide more information regarding the processing of related ceramics, the SiAlONs. The $Al_2O_3$ and AlN rich ends of this system are themselves potential candidates for high technology applications[26]. For example, the AlN rich compositions are being considered as candidates for electronic packaging applications, due to the high thermal conductivity and good mechanical properties of AlN. However, densification of AlN has been a difficult problem. Addition of small amounts of $Al_2O_3$ to AlN leads to the formation of a series of polytypoids, due to the insertion of a chemically distinct layer into another chemically distinct structure. These phenomena also occur in the alkali earth ceramic superconductors as noted earlier, **Figs.6(a&b)**. AlN has the 2H wurtzite structure, shown in **Fig.19(a)**, the cation:anion ratio being 1. As this value decreases, due to the addition of $Al_2O_3$, more of the tetrahedral sites in the wurtzite structure are occupied. This, however, leads to configurations where adjacent tetrahedra share a common base, causing the occurrence of rather short anion-anion distances. This is avoided by changing the cation arrangement locally to cubic, thus creating a stacking fault, shown schematically in **Fig.19(b)**. The local cubic layer has the composition of $MX_2$,

where M is the cation and X, the anion. The spacing of these faults is determined by the overall composition, i.e., the amount of $Al_2O_3$. Thus, the repeat sequence of these polytypoids can be used as an accurate local composition scale, i.e., the image periodicity directly reflects the M/X ratio. **Figs.20(a-c)**[27,28] show results of a typical set of experiments in which HREM, CBED and xray microanalysis with an UTW detector have been used to identify the structural details of the polytypoids in this system. **Fig.20(a)** is the lattice fringe image of the 32H polytypoid, along with the SAD pattern in the inset. Xray microanalysis data, **Fig.20(b)**, obtained with experimental k-factors and after correction for absorption, confirms the cation : anion ratio to be 16:17. The atomic resolution image in **Fig.20(c)** however shows the same 32H region to consist of intergrowths of the 21R and the 27R structures. Atomic resolution imaging, in this case is useful in obtaining supporting evidence for the microanalysis data, since the composition can be directly inferred from the stacking sequence in the HREM image, as summarized in **Table I**. Microanalytical quantification of oxygen and nitrogen has to be done with care. In **Fig.20(b)** one typical example is presented which illustrates the limitations of using system generated theoretical k-factors[29].

Table 1: Polytypoid structures generated with different cation:anion (M/x) ratios. These are observed in Al-O-N as well as Si-Al-O-N systems.

| n | M/x | Polytype | c(Å) |
|---|---|---|---|
| 4 | 4/5 | 8H | 23.04 |
| 5 | 5/6 | 15R | 41.85 |
| 6 | 6/7 | 12H | 32.88 |
| 7 | 7/8 | 21R | 57.12 |
| 8 | 8/9 | 16H | 40.70 |
| 9 | 9/10 | 27R | 72.09 |
| 11 | 11/12 | 33R | 86.46 |
| 12 | 12/13 | 24H | Not measured |
| 13 | 13/14 | 39R | 101.40 |
| 16 | 16/17 | 32H | 82.82 |
| ∞ | 1 | 2H | 4.98 |

The quantified data, using theoretical k-factors, is very different from the stoichiometric composition. The correct stoichiometry is not obtained even using experimental k-factors. It is necessary to apply the absorption corrections to the xray intensity of the nitrogen peak in order to obtain the correct composition. Thus it is essential to know the foil thickness with a fair degree of precision. CBED is very useful in this aspect, since the foil thickness, within the probe diameter can be obtained. Alternatively, the thickness can be estimated by energy loss spectroscopy. Such absorption corrections become more and more critical as the concentration of heavy elements in the matrix increases, for example, the BCSCO superconductors. One simple method to carry out microanalysis in such cases is to obtain spectra from points along a line that is normal to the edge of the foil. In this case, depending upon the wedge angle, the thickness will progressively increase. The exact location of the probe can be determined by the carbon contamination spot on the foil. The quantified data for the different points can be plotted against the distance of that data point from the edge. The composition, for an infinitely thin sample can then be obtained by extrapolating to zero ( i.e., the edge of the foil).

## SUMMARY

It is realized that in this short review one cannot cover the whole range of electron microscopy techniques, as applied to modern ceramics. However, it is hoped that the examples shown here are representative of the significance of modern electron microscopy methods of atomic resolution imaging, diffraction and spectroscopy in the task of characterising and understanding typical ceramic materials. The ARM at Berkeley is currently unique in providing the highest resolution [(1.6Å) over a ±40° tilt range] of any instrument in the world. It is located at the National Center for Electron Microscopy at the Lawrence Berkeley Laboratory which is a user operated facility open to all qualified electron microscopists and funded by the U.S.Department of Energy.

## ACKNOWLEDGEMENTS

The authors wish to acknowledge the technical contributions of and discussions with Drs. M.A.O'Keefe, K.M.Krishnan, C.J.D.Hetherington, R.Kilaas and R.S.Rai. The continued attention to the high performance of the ARM by C.Nelson is also acknowledged. The research work on electronic ceramics and superconductors is supported by the Director, Office of Energy Research, Office of Basic Energy Sciences, Materials Science Division of the U.S.Department of Energy under contract No. DE-AC03-76SF00098. The work on structural ceramics is supported by the National Science Foundation through grant No. DMR 83-1317239.

## REFERENCES


1. G.Thomas and M.J.Goringe, "Transmission Electron Microscopy of Materials", John Wiley and Sons, New York, (1979).
2. T.A.Bielicki, U.Dahmen, K.H.Westmacott and G.Thomas, in Zirconia'86, Proc. of Int. Conf., Ed. S.Somiya, Tokyo, Japan ( in press).
3. R.Gronsky and G.Thomas, in Proc. of 41th Ann. Meeting of EMSA, Ed. G.W.Bailey, Claitor's, Baton Rouge(1983), p310.
4. W.O.Saxton and T.L.Koch, Jl. of Microscopy, 127, 69-75(1982).
5. R.Kilaas, in Proc. of 45th Ann Meeting of EMSA, Ed. G.W.Bailey, San Francisco Press, San Francisco, Ca (1987), p66-69.
6. M.A.O'Keefe and R.Kilaas, in Proc. of 6th Pfefferkorn Conf., Niagara Falls, NY, (1988), to be published in the proceedings.
7. K.M.Krishnan, P.Rez and G.Thomas, Acta Cryst., B41, 396(1985).
8. J.G.Bednorz and K.A.Muller, Z. Phys., B64, 189(1986).
9. R.Ramesh, G.Thomas, S.M.Green, C.Jiang, Yu Mei, M.L.Rudee and H.L.Luo, Phys. Rev., 38, 7070(1988).
10. C.J.D.Hetherington, R.Ramesh, M.A.O'Keefe, R.Kilaas, G.Thomas, S.M.Green and H.L.Luo, Appl. Phys., Lett., 53, 1016(1988).
11. D.R.Clarke, Jl. of Amer. Cer. Soc., 63, 208(1980).
12. T.M.Shaw and G.Thomas, Jl. of Solid State Chem., 33, 63(1980).
13. R.Ramesh, G.Thomas, S.M.Green, C.Jiang, Y.Mei and H.L.Luo, in Proc. of 1988 Applied Superconductivity Conf., San Francisco, CA, (1988).
14. H.W.Zandbergen, R.Gronsky and G.Thomas, Jl. de Microscopie et du Spectroscopie Electronique, (1988) in press.
15. R.Sadanaga, M.Tokonami and Y.Takeuchi, Acta Cryst., 15, 65(1962).
16. D.Schryvers, K.Srikrishna, M.A.O'Keefe and G.Thomas, Jl. of Materials Research, in press.
17. K.H.Jack, in Proc. of NATO Advanced Study Institute, Ed. F.L.Riley, Noordhoff Publishers, 1977.
18. D.R.Clarke and G.Thomas, Jl. of Amer. Cer. Soc., 61, 114(1978).
19. R.E.Loehman, Jl. of Amer. Cer. Soc., 62, 491(1979).
20. G.Thomas, C.Ahn and J.Weiss, Comm. of Amer. Cer. Soc., 65, 185(1982).
21. T.M.Shaw, G.Thomas and R.E.Loehman, Jl. of Amer. Cer. Soc., 67, 643(1984).
22. G.Thomas, in Ceramic Microstructures, Ed. J.A.Pask and A.G.Evans, Plenum Publishers, 1988, pp55-72.
23. T.R.Dinger, R.S.Rai and G.Thomas, Jl. of Amer. Cer. Soc., (1988), in press.
24. R.S.Rai, M.A.O'Keefe and G.Thomas, in Proc. of MRS Symp., Vol.82, 429(1987).
25. M.A.O'Keefe, R.S.Rai and G.Thomas, to be presented at the MRS Symp. on High Resolution Electron Microscopy, Boston, MA, Nov., 1988.
26. N.D.Corbin and J.W.McCauley, in Proc. of the Soc. of Photo-Optical Inst. Engineers, 297, 19(1981).
27. K.M.Krishnan, R.S.Rai, G.Thomas, N.D.Corbin and J.W.McCauley, in Proc. of MRS Symp., Vol.60, 211(1986).
28. K.M.Krishnan and G.Thomas, in Proc. of Microbeam Analysis-1987, Ed. R.H.Geiss, San Francisco Press, San Francisco, CA, pp222-224.
29. K.M.Krishnan, unpublished work.

## FIGURE CAPTIONS

Figure 1: A schematic showing the different types of information that can be obtained from a modern transmission electron microscope, and some of the problems associated with the preparation and imaging of thin foils prepared from the bulk.

Figure 2: A plot of $C_s$, the spherical aberration coefficient versus resolution, for different accelerating voltages. Note that for a typical $C_s$ value of 3mm, to obtain a resolution of 2Å, the accelerating voltage has to be in the range of 500-1000kV. ( Courtesy of J. Wiley and Sons, New York).

Figure 3: (a) Plots of the contrast transfer function at Scherzer defocus for two accelerating voltages, 400kV and 1MeV ;(b) computer generated images of orthorhombic $ZrO_2$ for varying specimen thickness and objective defocus. Notice the large variations in the image detail. (Courtesy R.Kilaas).

Figure 4: (a) [110] ARM image of the n=3[$T_c$=110K] polytypoid in the Bi-Ca-Sr-Cu-O system ; (b)image in (a) after SEMPER processing. Note the intensity difference in the central Cu-O row compared to the other two rows.(Courtesy Appl. Phys. Lett.)

Figure 5: (a) [110] projected potential for the perfect n=3 structure ; (b) simulated images corresponding to (a) ; (c) projected potential for a structure where the oxygen from the central Cu-O row has been removed ; (d) simulated images corresponding to the structure in (c) showing the intensity difference between the central Cu-O row and the other two rows. (Courtesy Appl. Phys. Lett.).

Figure 6: (a) Lattice fringe image near the grain boundary of the un-leaded sample, showing the change in composition ( and $T_c$) from that of n=3 to n=1 ; (b) lattice fringe image in the case of a leaded sample, showing the uniform composition of n=3 up to the grain boundary.(Courtesy Phys. Rev. B).

Figure 7: Lattice fringe image showing polytype formation adjacent to a grain boundary in MgSiAlON. (Courtesy Jl. Amer. Cer. Soc.).

Figure 8: High resolution image, simulated image and structural model illustrating the formation of different polytypes in Be-Si-N.

Figure 9: (a) HREM image of a grain boundary in Y-Ba-Cu-O ceramic ; (b) SEMPER processed image in which the upper grain in the [100] zone axis has been processed to reveal the grain boundary plane to be a Ba-O plane.(Courtesy H.Zandbergen).

Figure 10: HREM image of a Bi-Ca-Sr-Cu-O thin foil whose edge has been damaged due to electron beam and Argon ion beam irradiation.

Figure 11: Structural model of mullite in the [001] orientation.

Figure 12: (a&b) Simulated images of mullite for a foil thickness of 29Å and for defocus values of 0Å and -100Å respectively ; (c) ARM image corresponding to the simulated images in (a&b).(Courtesy Jl. of Materials Research).

Figure 13: (a&b) Simulated images of mullite for a foil thickness of 87Å and for defocus values of 0Å and 100Å respectively ; (c) ARM image of

comparable foil thickness, showing the image details to match well with those in the simulated images.(Courtesy Jl. of Materials Research).

Figure 14: (a) ARM image of mullite, whose Fourier transform is shown in (b). Note the small tilt from the exact zone axis. (c) image of the same region as in (a), but after processing by tilting the foil in the computer, the Fourier transform for which is shown in (d).(Courtesy Jl. of Materials Research).

Figure 15: (A-E) Schematic diagrams of the grain boundary microstructures that can evolve in liquid phase sintered ceramics.

Figure 16: Isothermal section of the AlN-$SiO_2$-$Y_2O_3$ phase diagram.(Courtesy Jl. Amer. Cer. Soc.).

Figure 17: (a) HREM image of the interface between the $\delta_1$-$\delta_2$ dendrites showing flat interfaces, with strain contrast only at the ledges.(Courtesy Jl. of Amer. Cer. Soc.) ; (b) atomic resolution image of the $\delta_1$ $Y_2Si_2O_7$ phase along with the simulated image, showing a good fit ( notice the slight skew, probably due to a small tilt of the sample).

Figure 18: (a) Un-processed image of the $Y_2Si_2O_7$ phase near the amorphous edge, showing no discernible structural detail ; (b) un-processed image of the same crystal as in (a), but in a thicker region, showing some structural detail, but lacking in the symmetry details ; (c) processed image corresponding to (a) showing the intrinsic structure present in the image as well as the correct symmetry of the crystal ; (d) processed image corresponding to (b), showing again the influence of sample misorientation on the thicker regions ; (e) processed image from the thin region, overlaid on the simulated image, showing an excellent match (Courtesy Materials Research Society and M.A.O'Keefe).

Figure 19: (a) The 2H wurtzite structure of AlN ; (b) structural model showing the formation of a stacking fault in the wurtzite structure.

Figure 20: (a) Lattice fringe image of the 32H polytypoid along with the SAD pattern in the inset ; (b) EDX spectrum along with the quantified data that determines the cation : anion ratio to be 16:17 ; (c) atomic resolution image showing the actual structure of the 32H polytypoid to be an intergrowth of the 21R and the 27R structures.(Courtesy San Francisco Press).

# CHARACTERIZATION BY ELECTRON MICROSCOPY

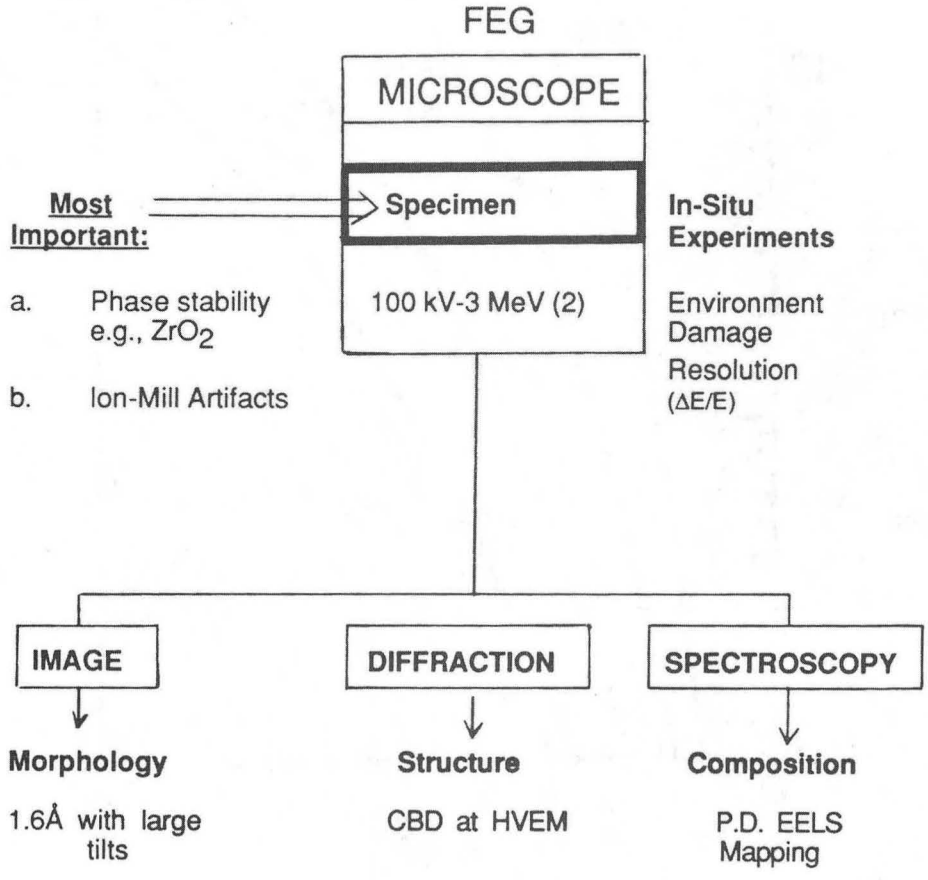


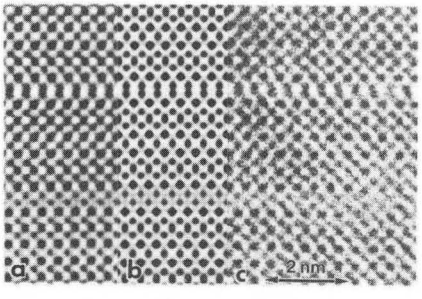


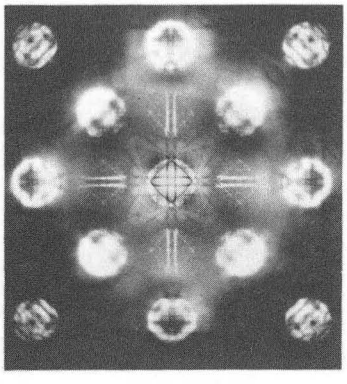

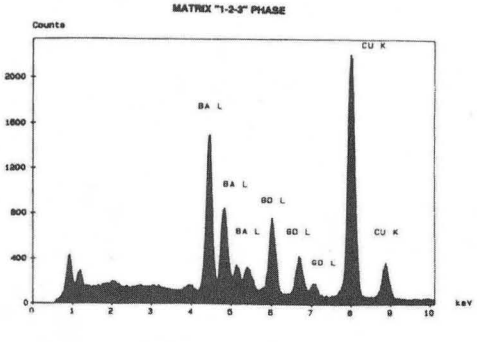


XBB 882-1149

Fig. 1

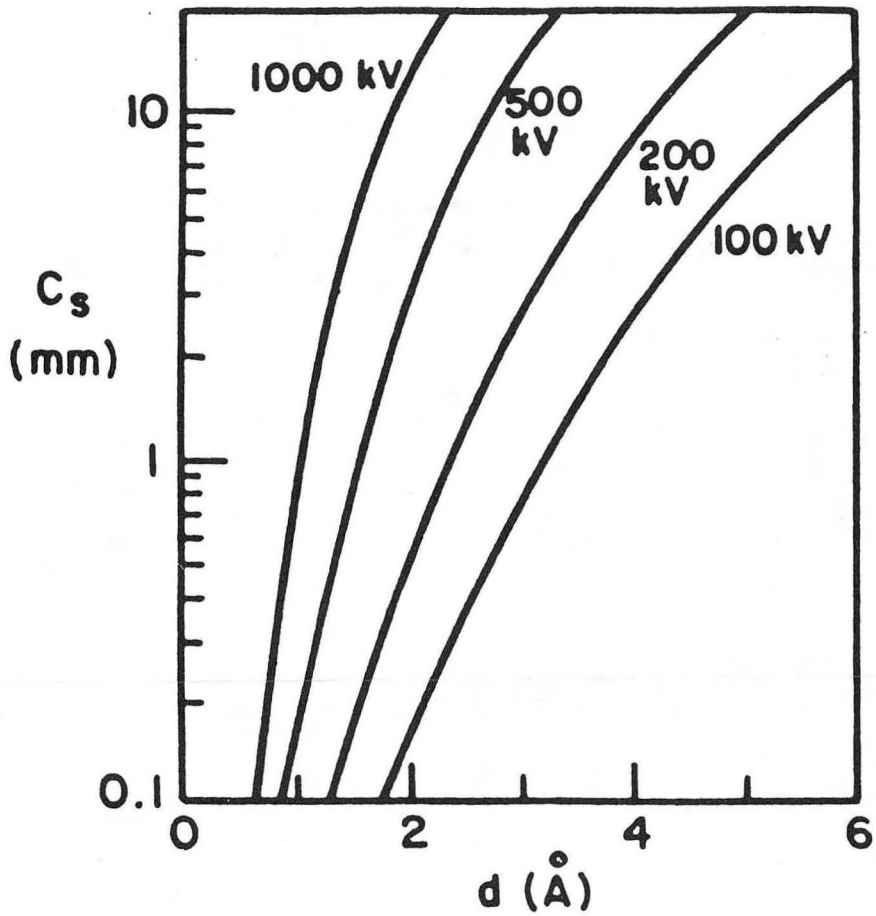


XBL 7810-5896

Fig. 2

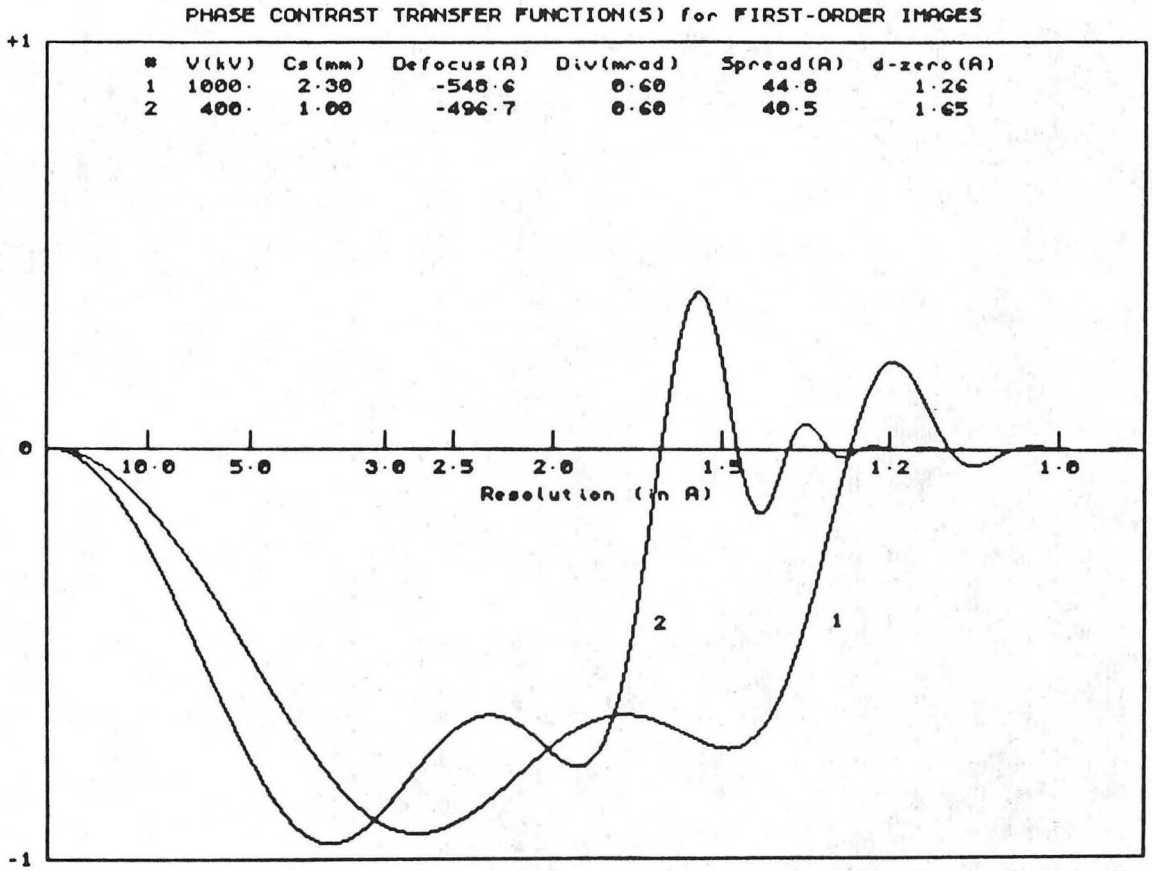


XBL 8812-4347

Fig. 3a

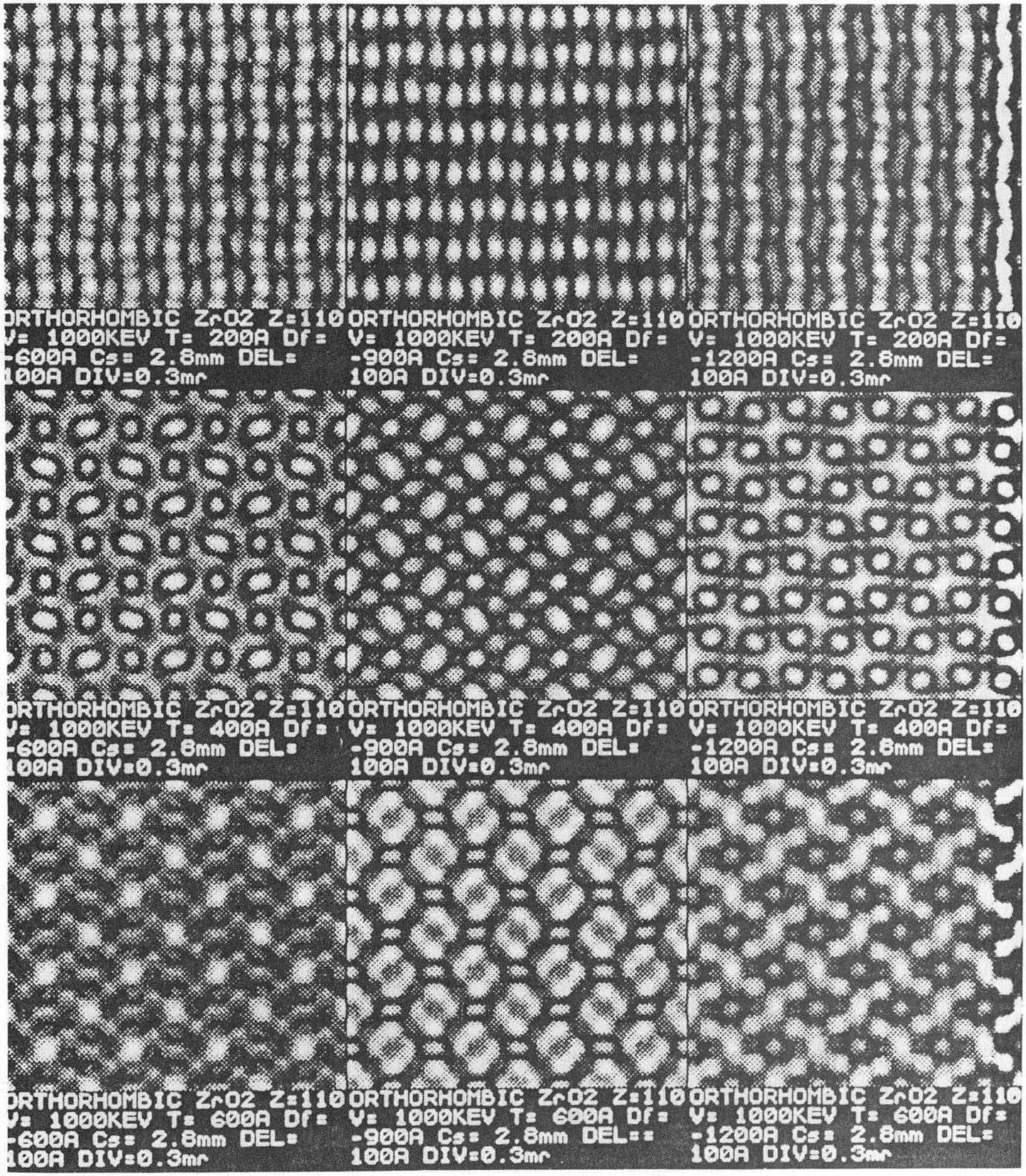


XBB 880-11779

Fig. 3b

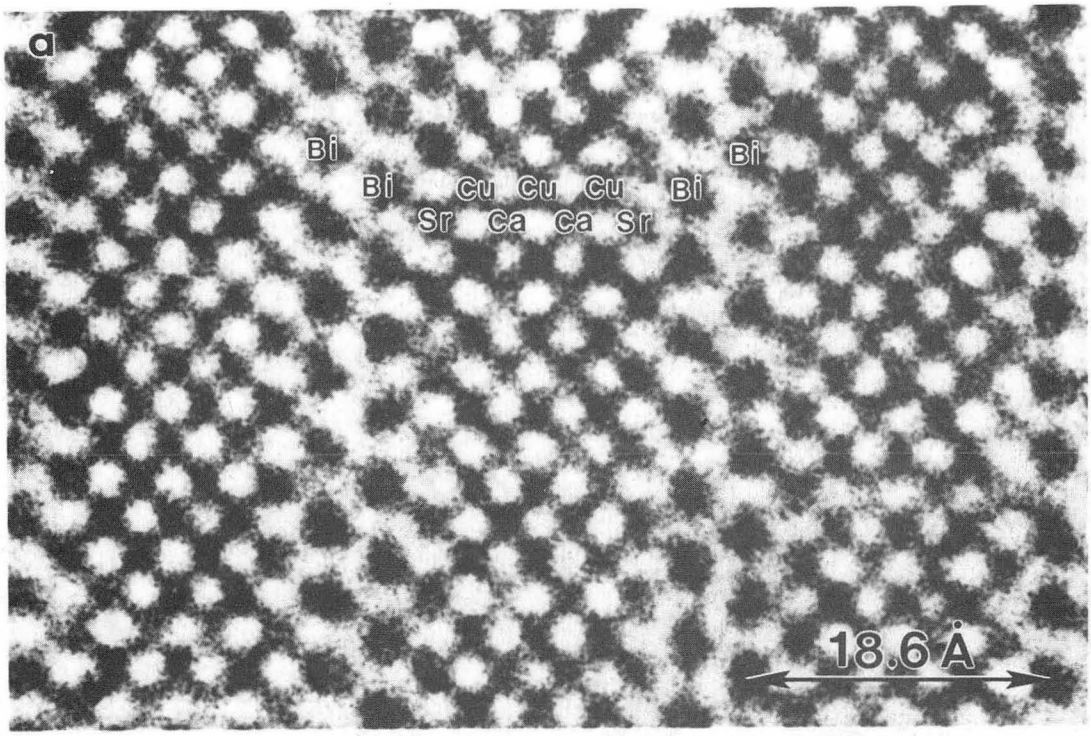


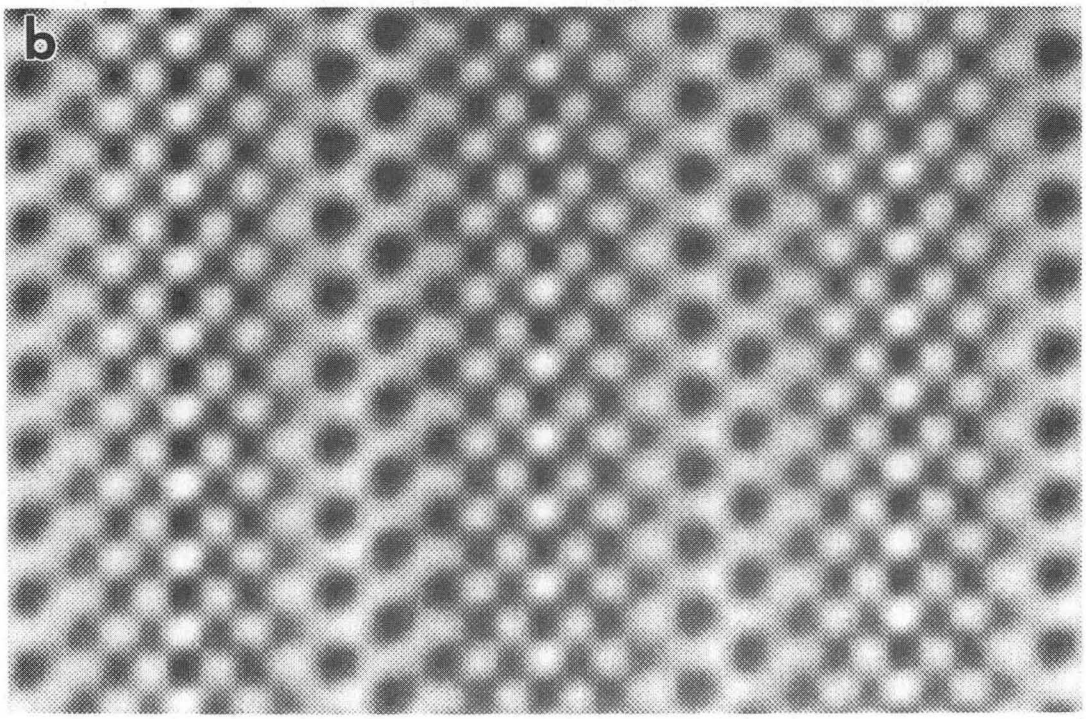


**$Bi_2Sr_2Ca_2Cu_3O_y$ (2-2-2-3)** **$T_c$ = 110K** **c=37.2Å**

XBB 885-4984A

Fig. 4

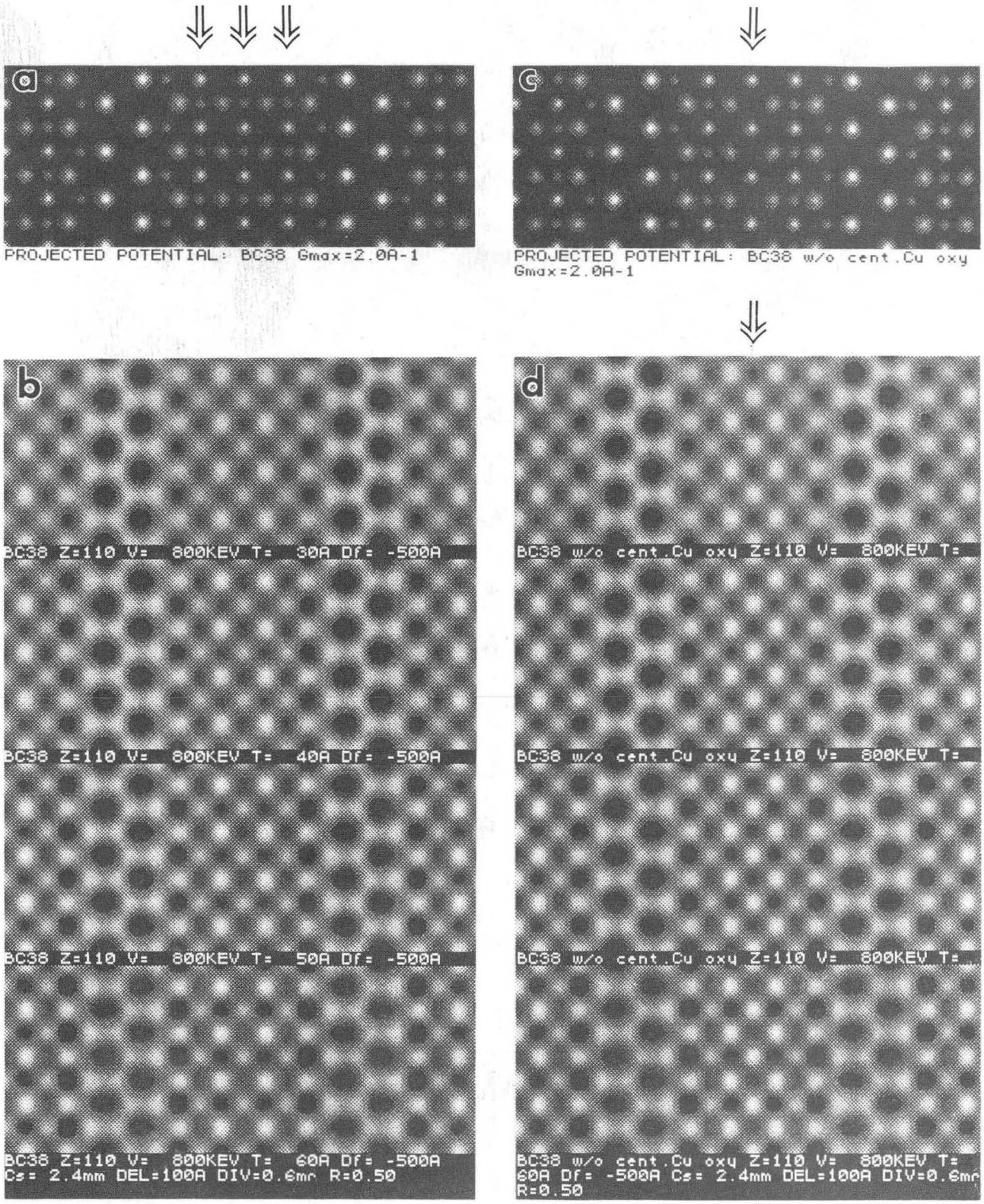


XBB 885-4983

Fig. 5

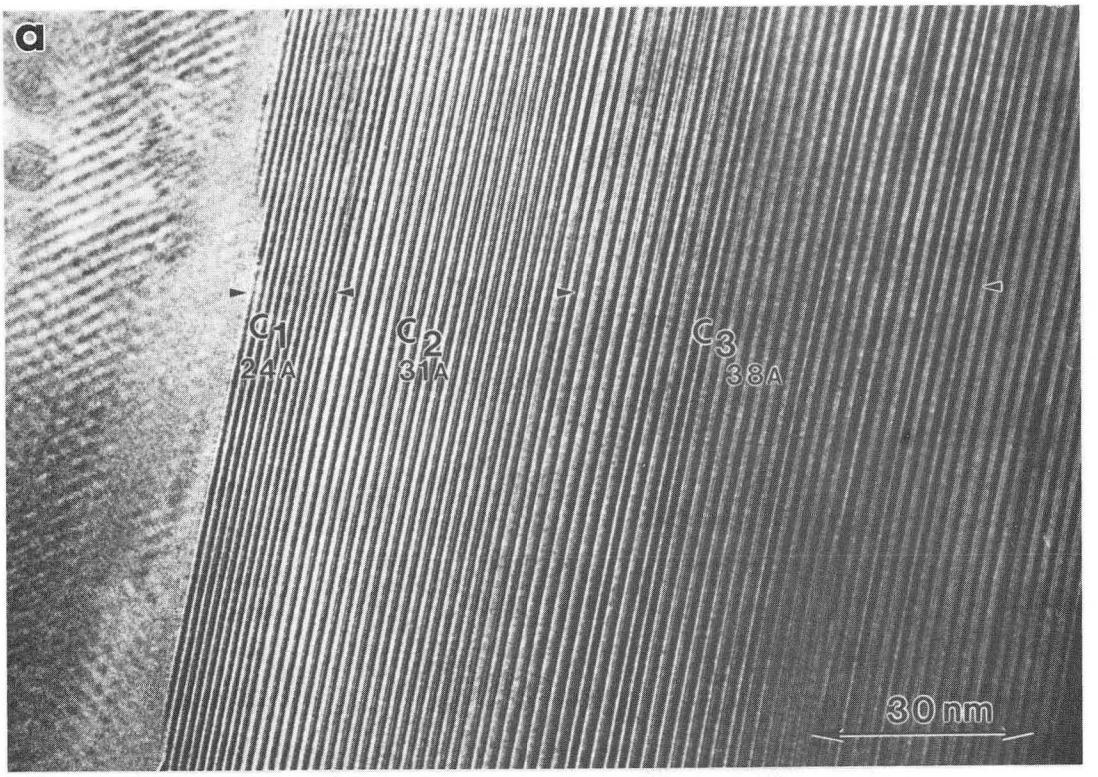


XBB 885-4701

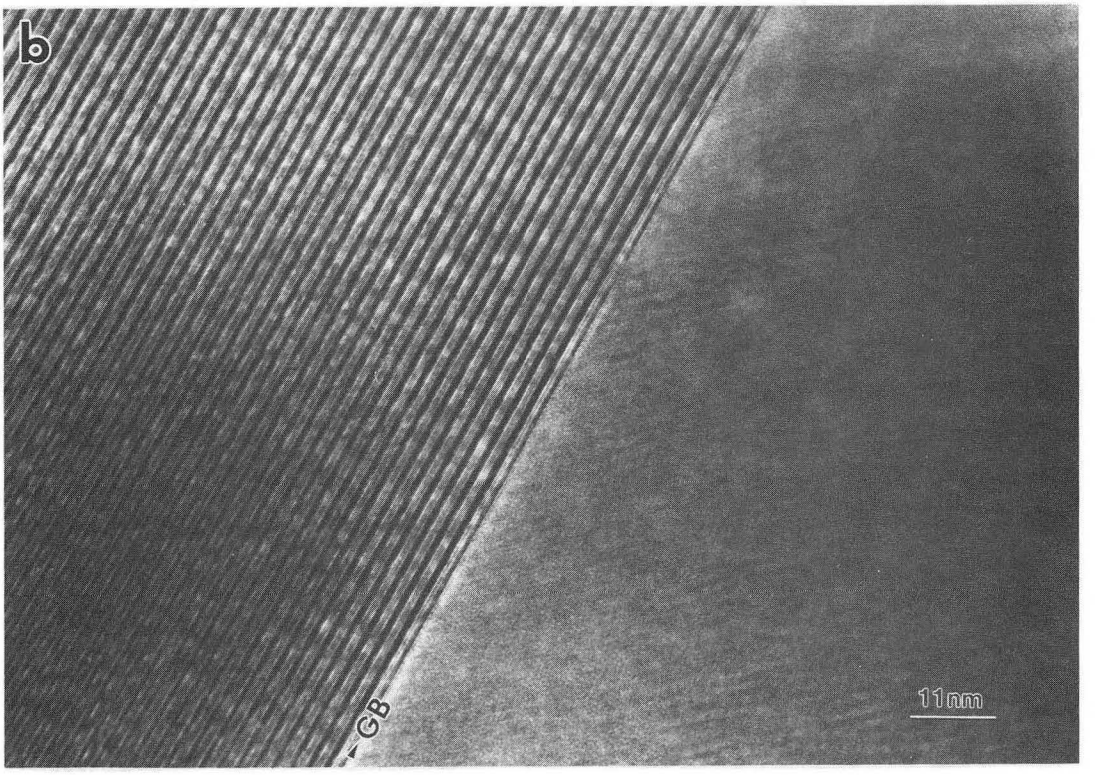


XBB 888-7843

Fig. 6

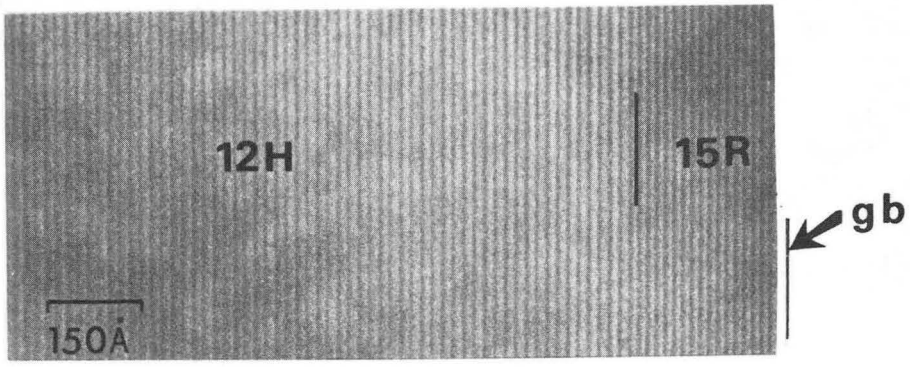


XBB 786-6929

Fig. 7

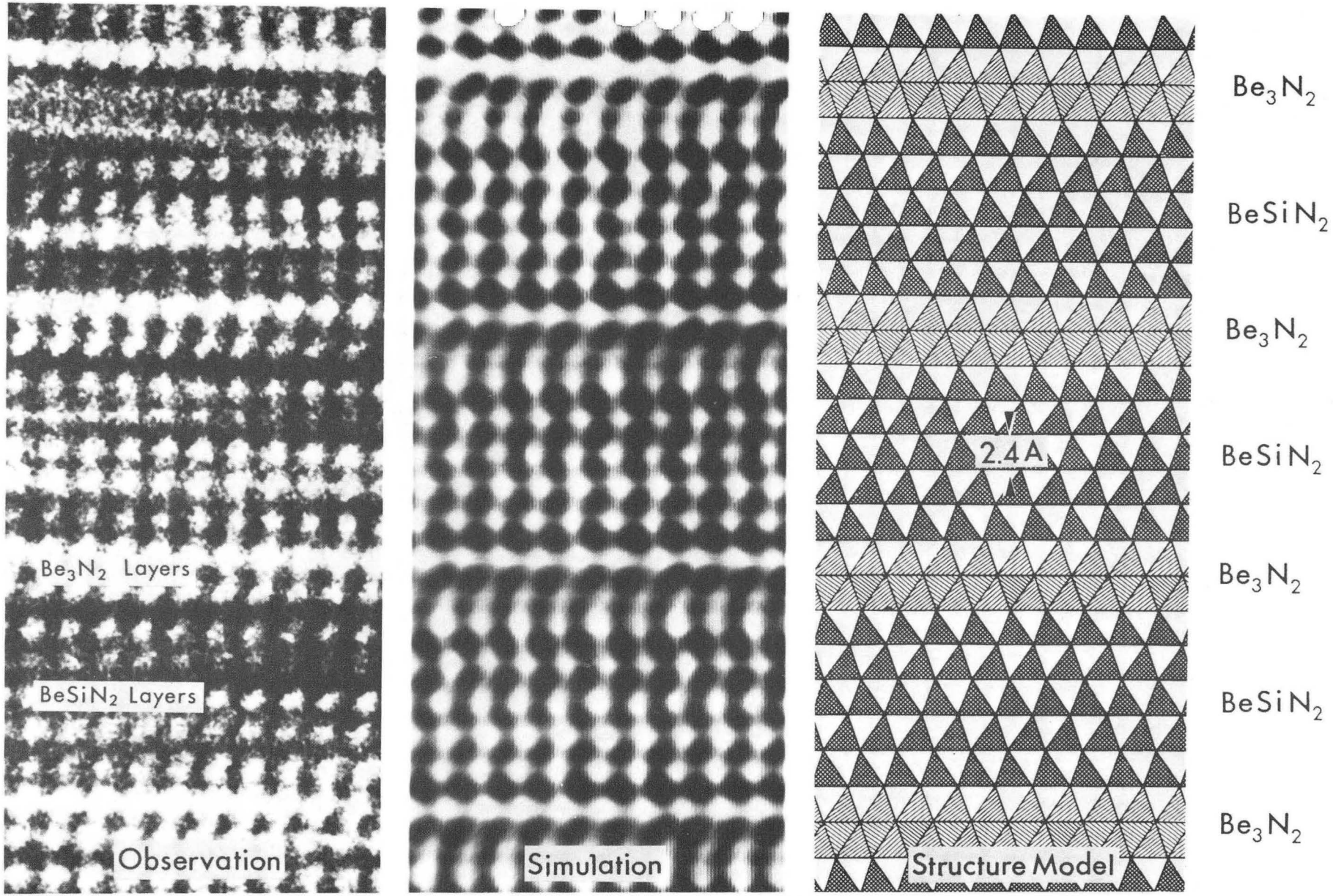


XBB 8810-9667

Fig. 8

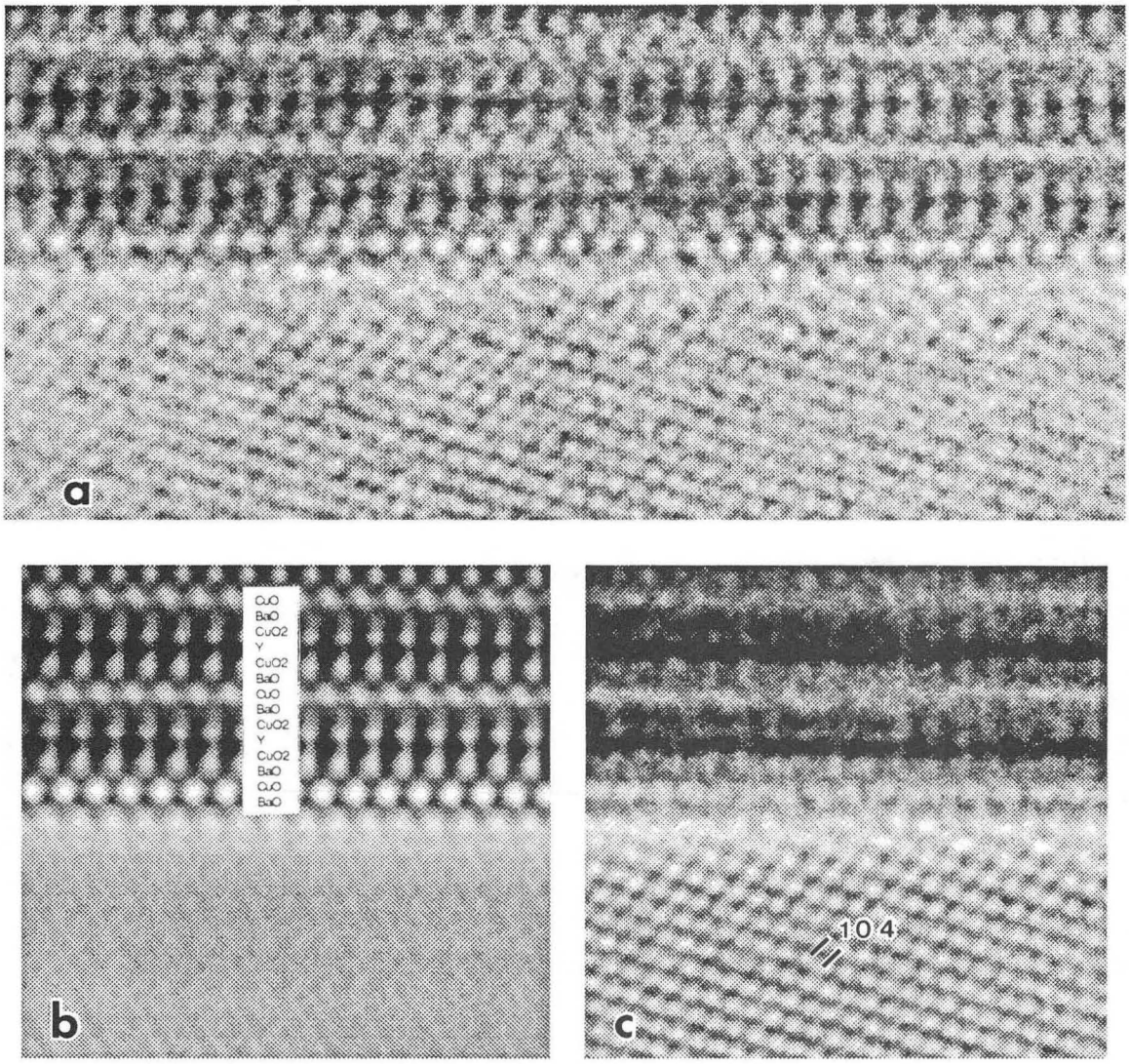


XBB 891-60

Fig. 9

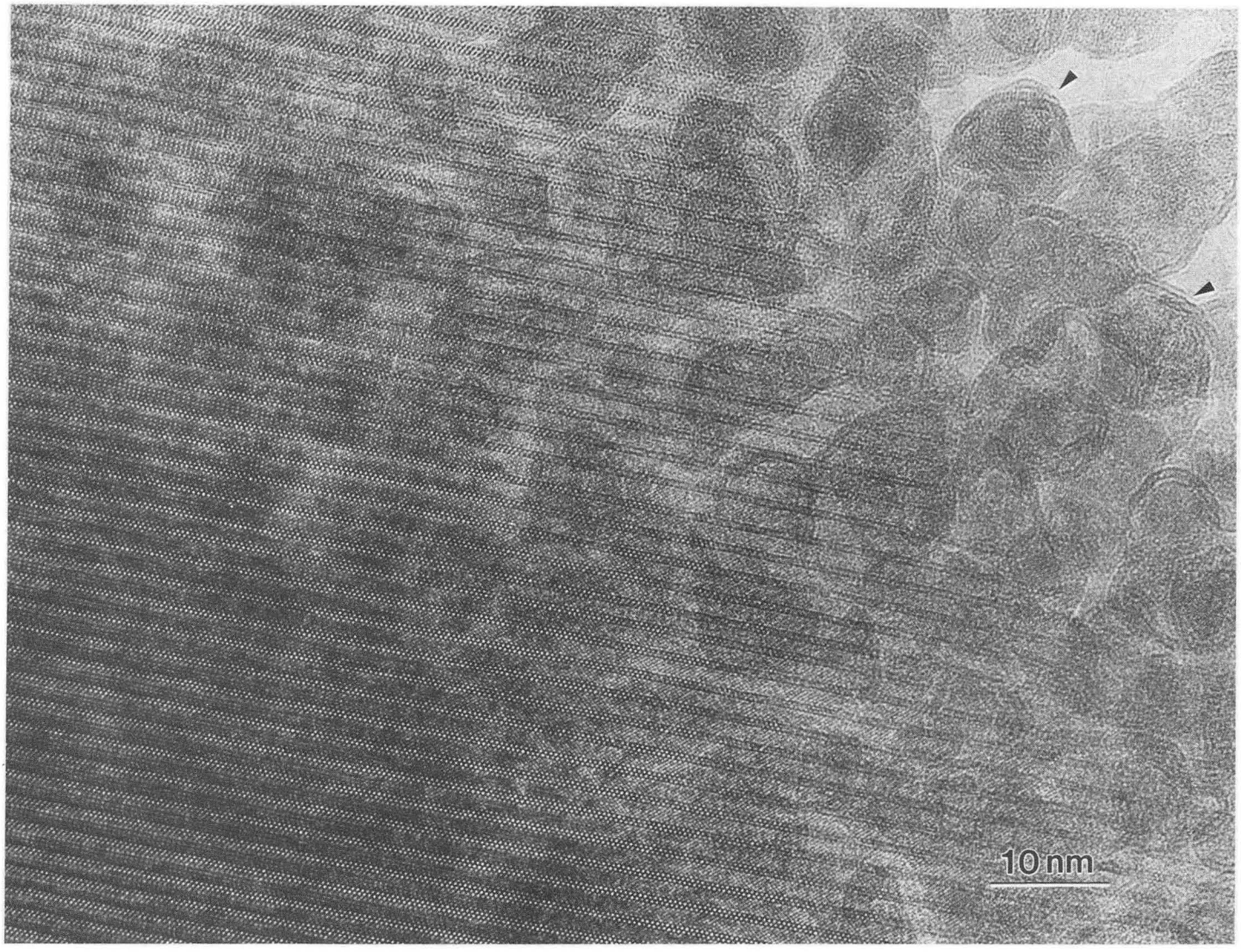


XBB 8810-10359

Fig. 10

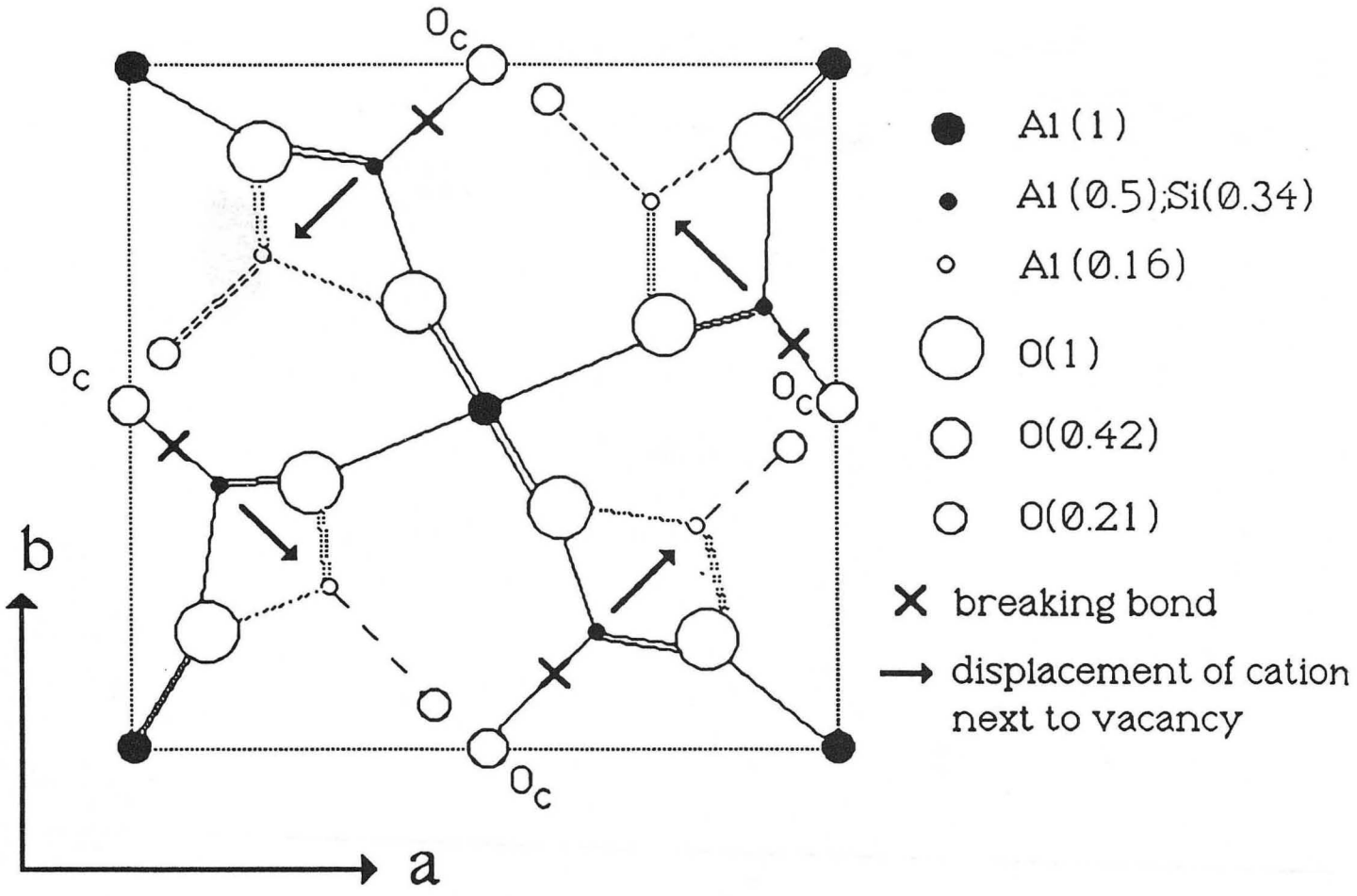


XBL 883-811

Fig. 11

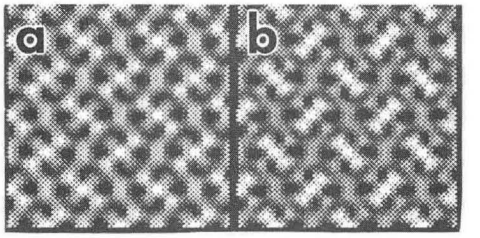


XBB 882-1201

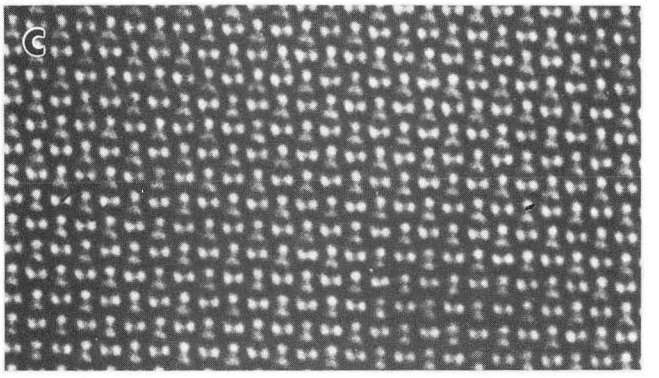


XBB 882-1196A

Fig. 12

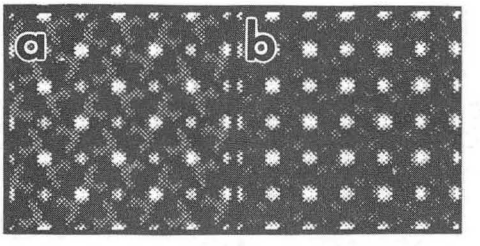


XBB 882-1201

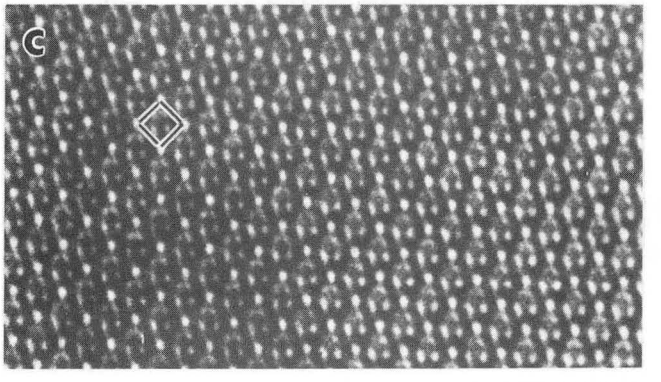


XBB 882-1196A

Fig. 13

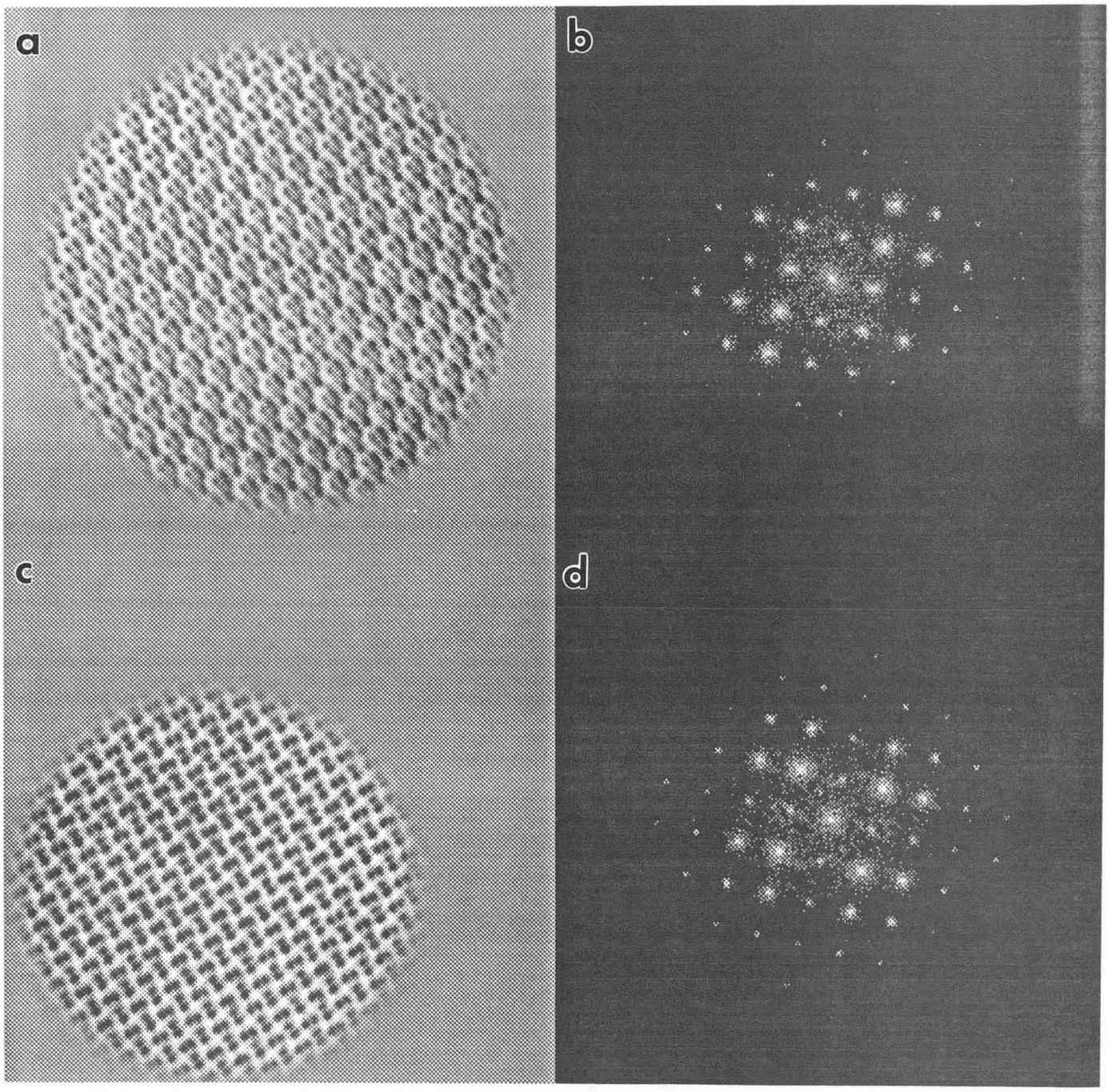


XBB 882-1198

Fig. 14

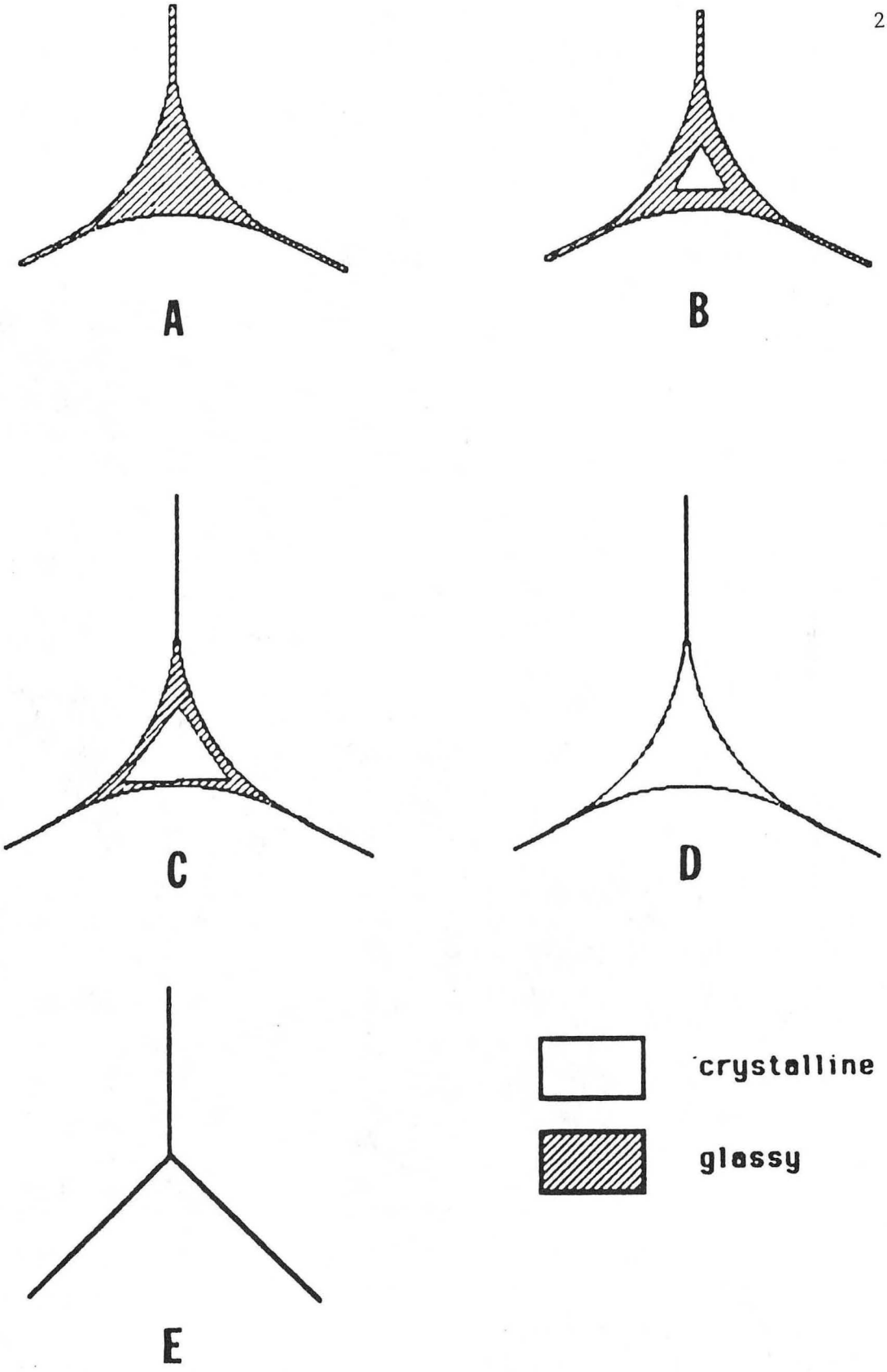


XBL 868-2983

Fig. 15

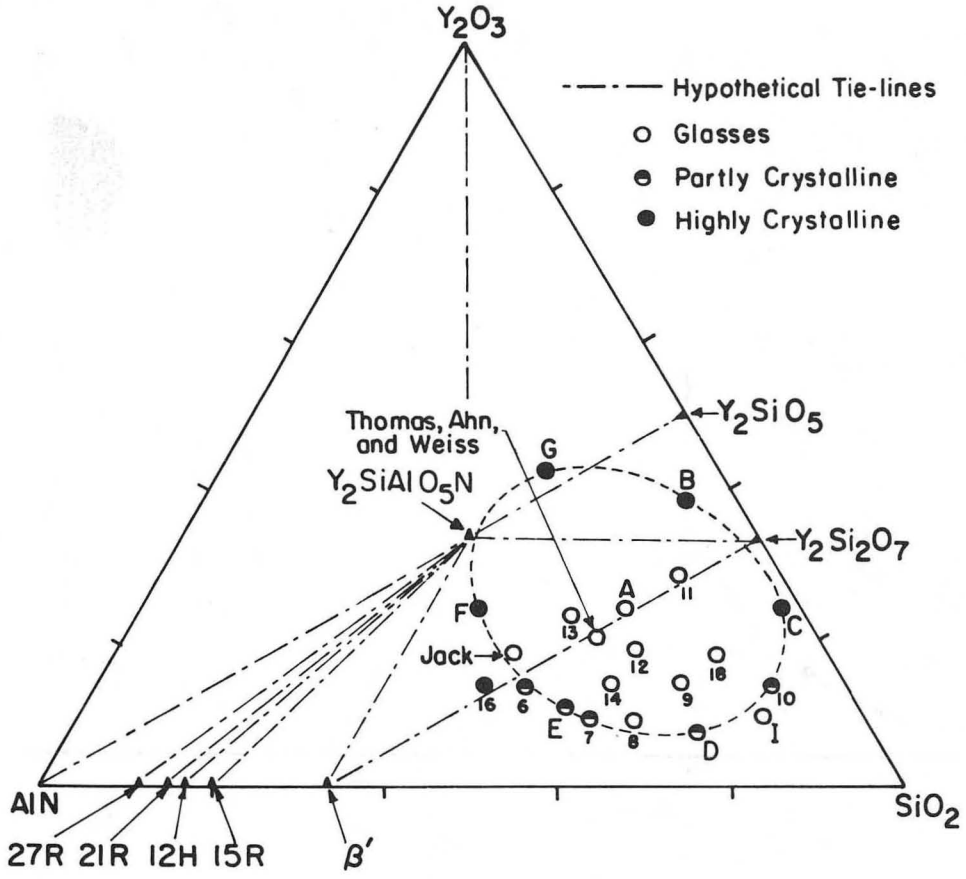


XBL 835-9790

Fig. 16

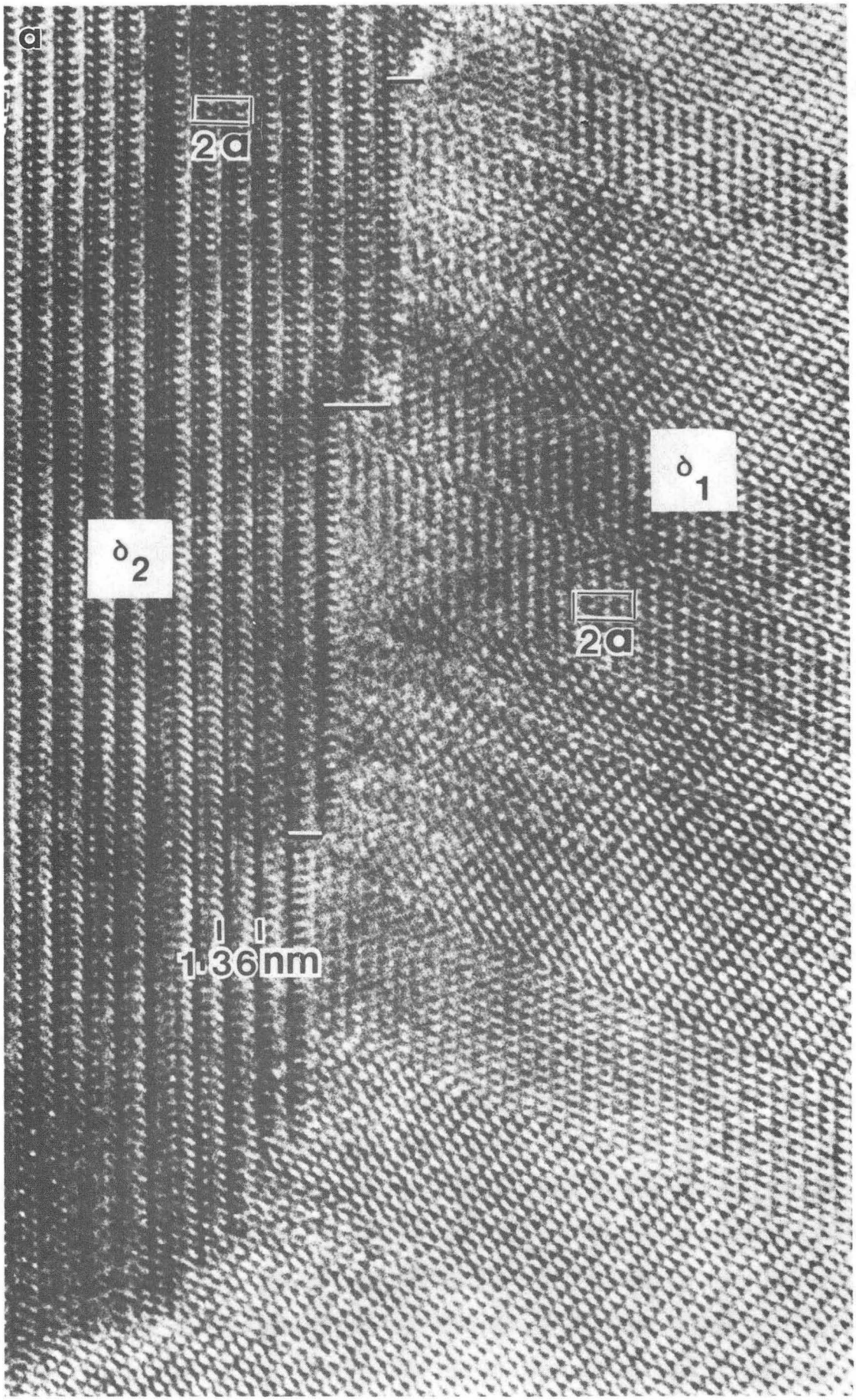


XBB 8610-8042

Fig. 17a

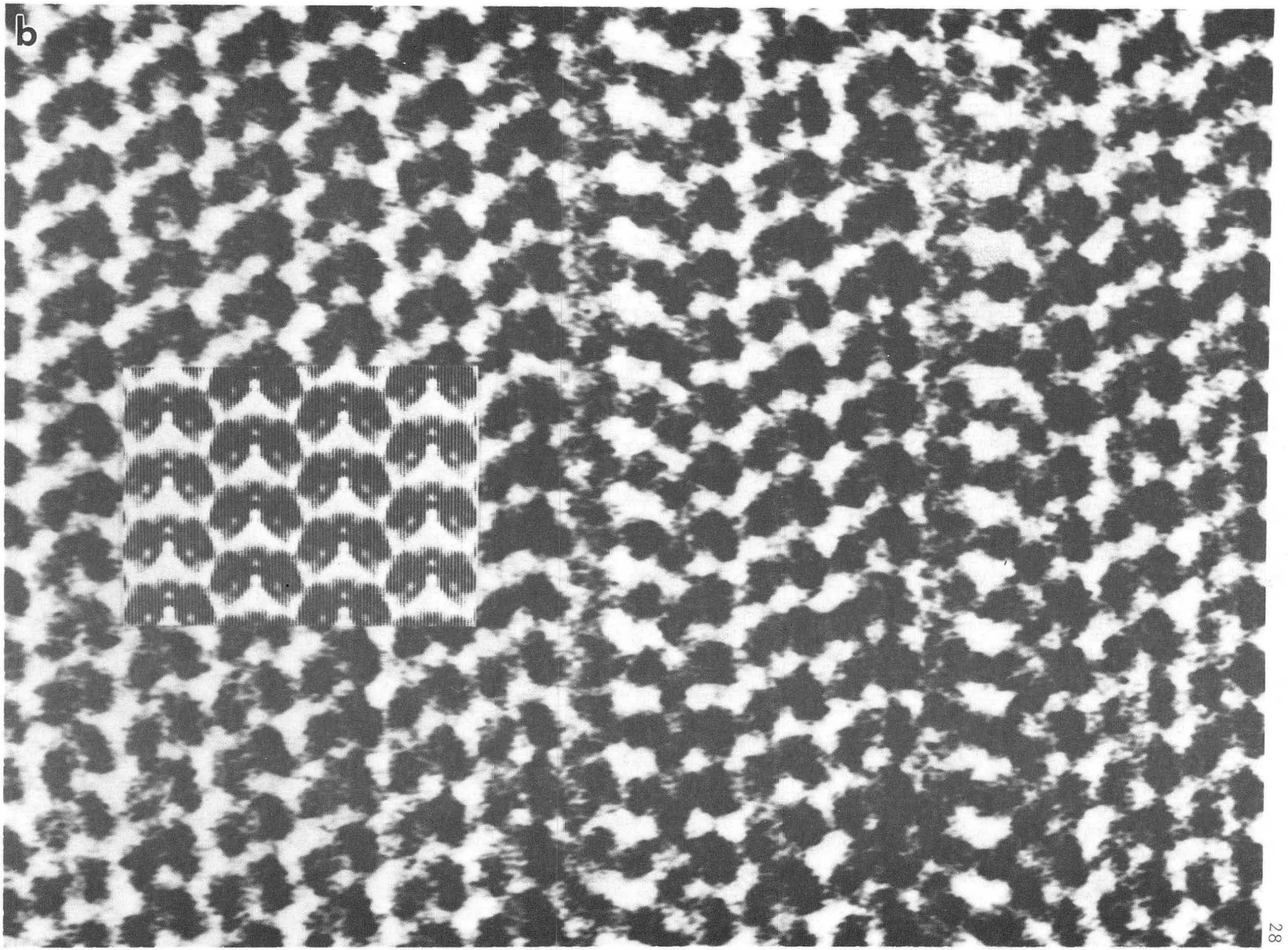


XBB 8610-8041

Fig. 17b

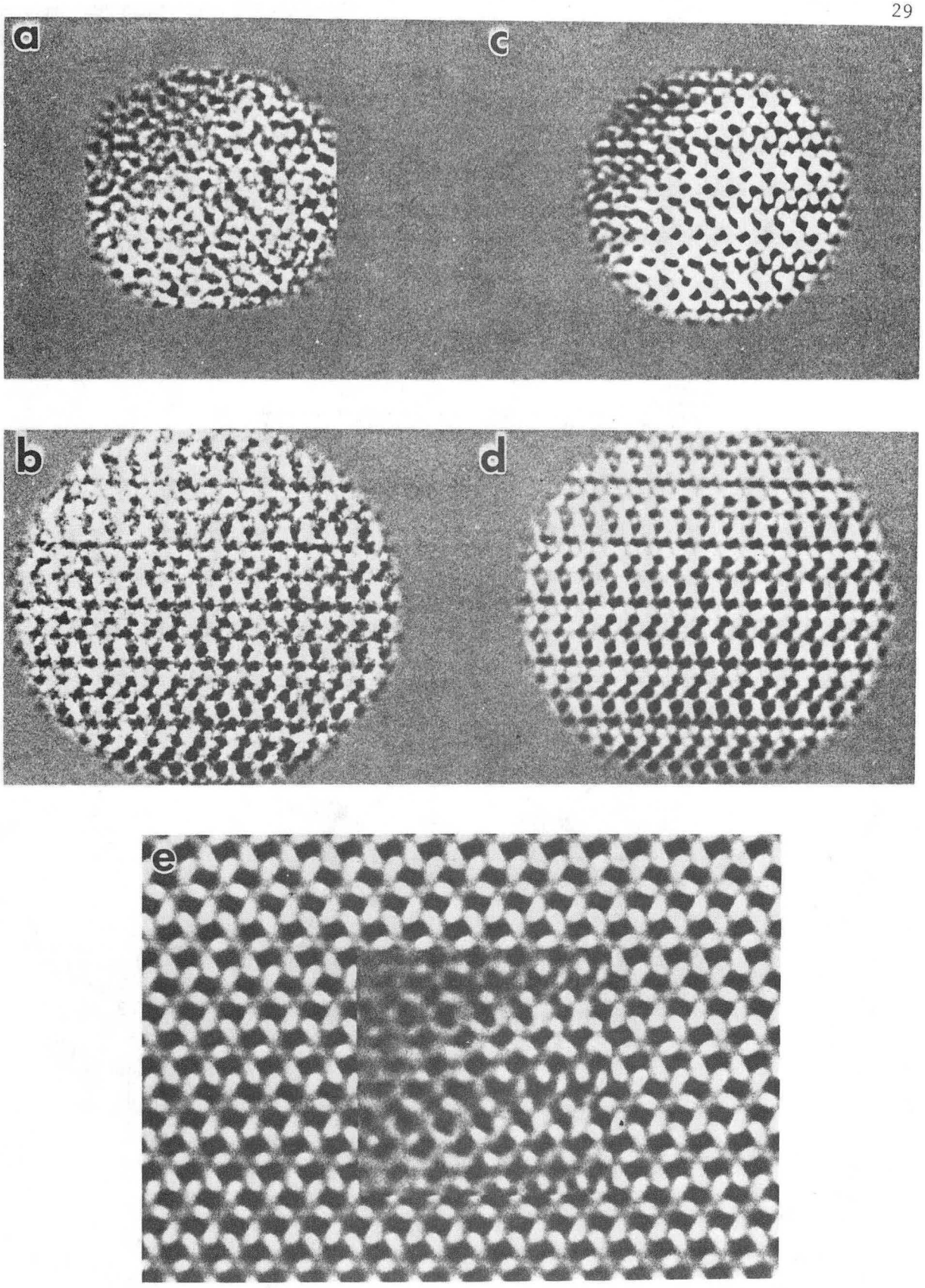


XBB 880-11780

Fig. 18

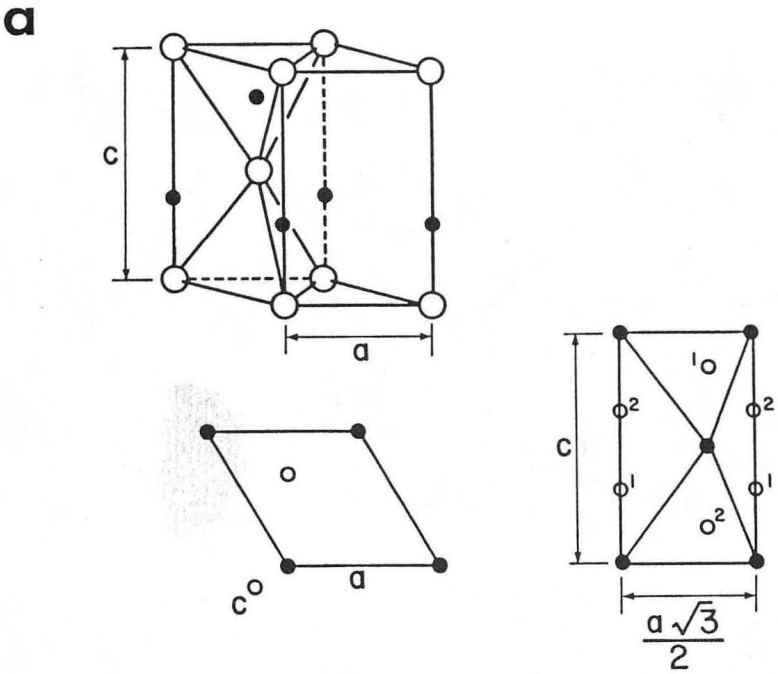


XBL 825-664

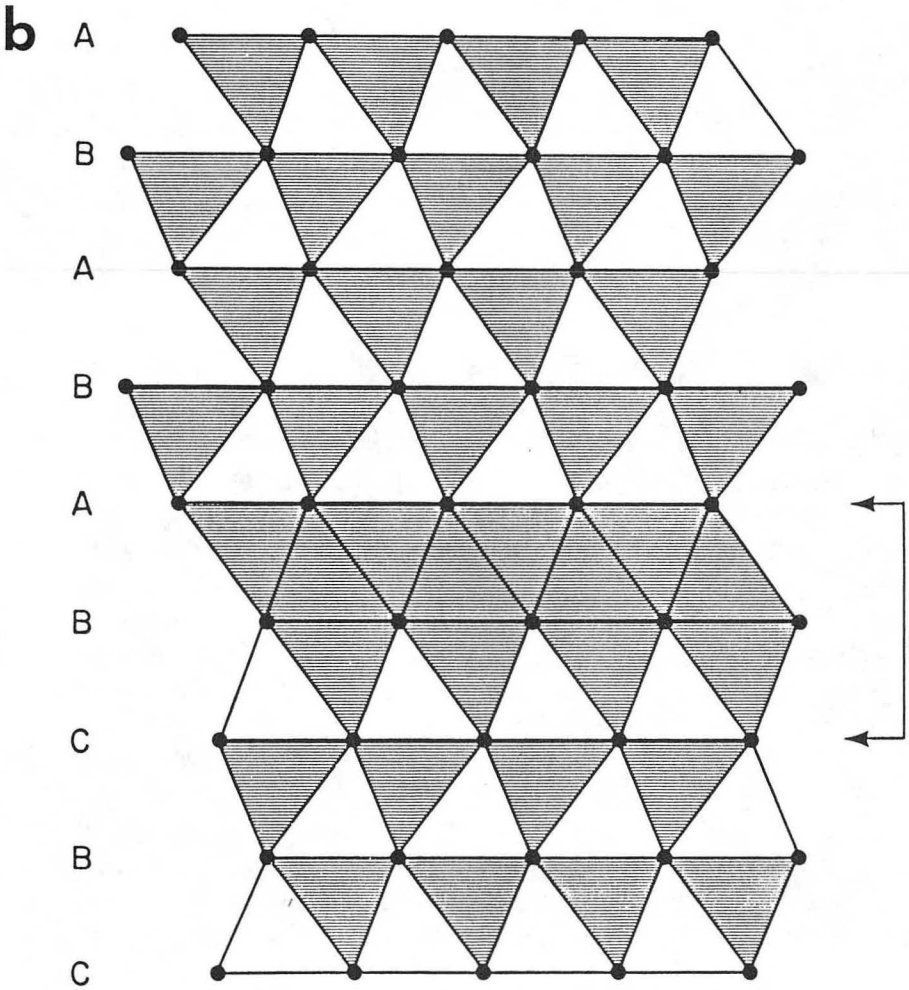


XBL 825-663

Fig. 19

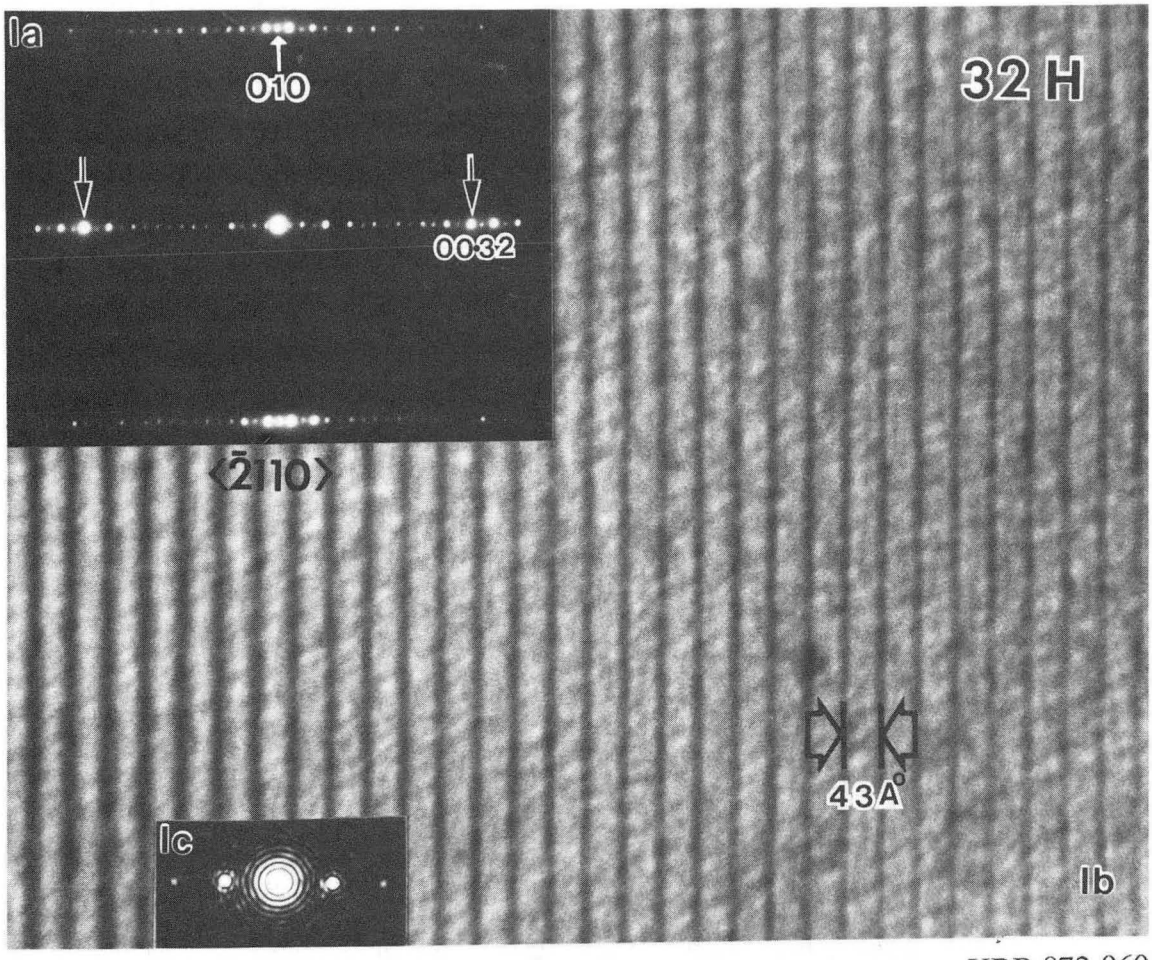


XBB 872-960

Fig. 20a

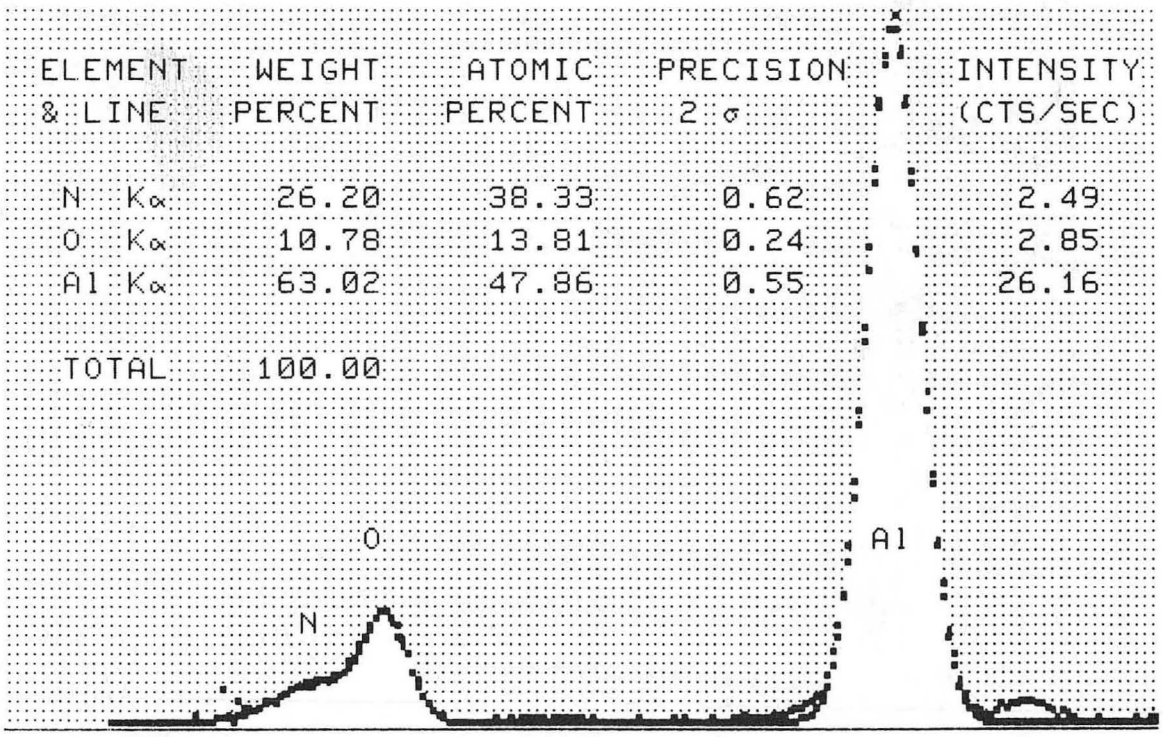


XBL 871-309

Fig. 20b

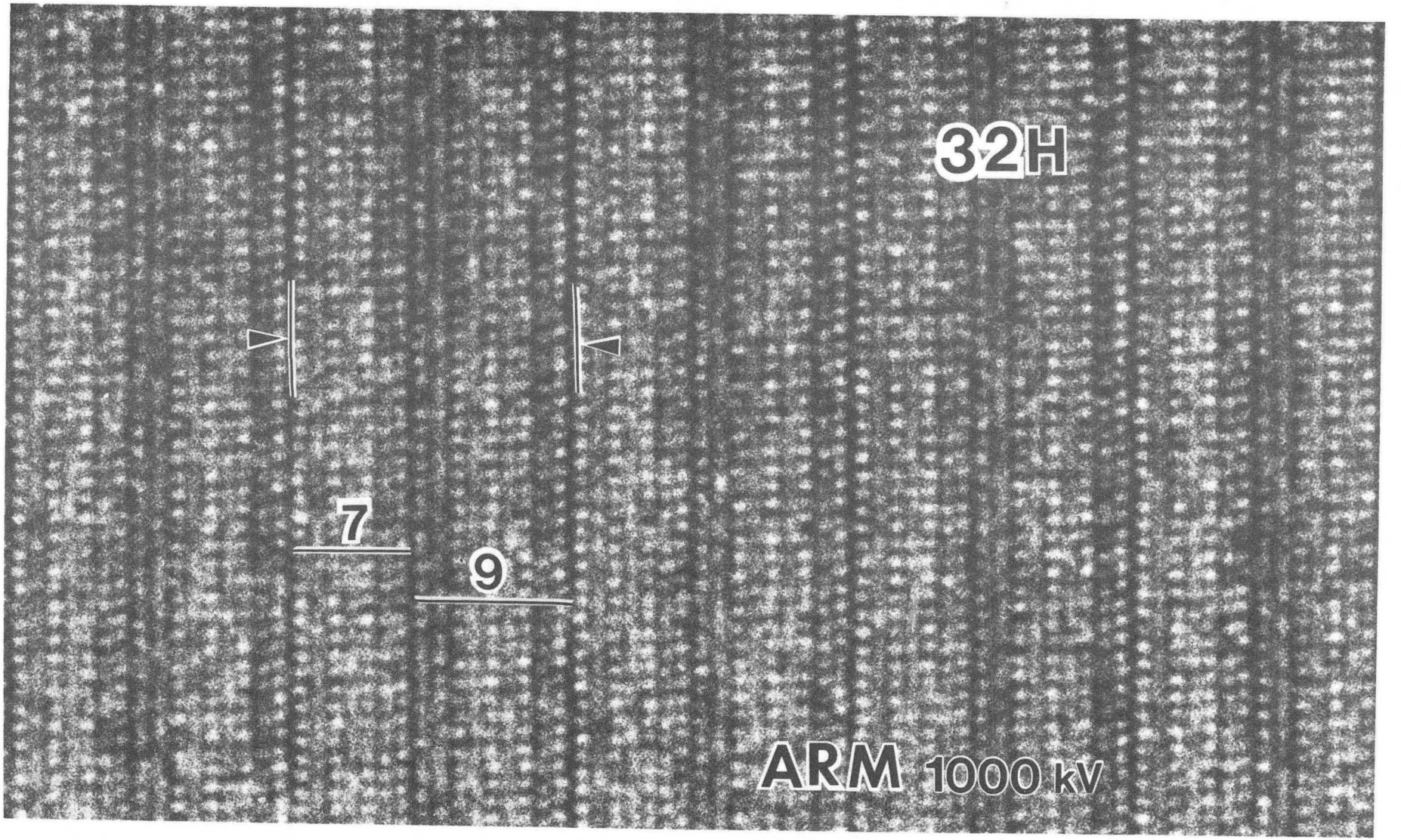


XBB 872-959



Fig. 20c

LAWRENCE BERKELEY LABORATORY
TECHNICAL INFORMATION DEPARTMENT
1 CYCLOTRON ROAD
BERKELEY, CALIFORNIA 94720